Multimodal delineation of a layer of effector function among exhausted CD8 T cells in tumors

Arja Ray[1,2], Molly Bassette[1,2], Kenneth H. Hu[1,2,#], Lomax F. Pass[1,2], Tristan Courau[1,2], Bushra Samad[2,3], Alexis Combes[1,2,3,5], Vrinda Johri[2,3], Brittany Davidson[2,3], Katherine Wai[6], Patrick Ha[6], Grace Hernandez[4], Itzia Zaleta-Linares[1,2], Matthew F. Krummel[1,2*]

Affiliations:
[1]Department of Pathology, [2]ImmunoX Initiative, [3]UCSF CoLabs, [4]Department of Anatomy, [5]Department of Medicine, [6]Department of Otolaryngology Head and Neck Surgery, University of California, San Francisco, CA 94143, USA. [#]Current Address: Department of Immunology, The University of Texas MD Anderson Cancer Center and James P Allison Institute

***Corresponding Author:**
Matthew F. Krummel, Ph.D.
513 Parnassus Avenue, HSW 512
San Francisco, CA 94143-0511
matthew.krummel@ucsf.edu
Tel: (415) 514-3130
Fax: (415) 514-3165

Abstract: The anti-tumor function of CD8 T cells is limited through well-established pathways of T cell exhaustion (T_{EX}). Strategies to capture emergent functional states amongst this dominant trajectory of dysfunction are necessary to find pathways to durable anti-tumor immunity. By leveraging transcriptional reporting (by the fluorescent protein TFP) of the T cell activation marker *Cd69,* related to upstream AP-1 transcription factors, we define a classifier for potent versus sub-optimal CD69+ activation states arising from T cell stimulation. In tumors, this delineation acts an additional functional readout along the T_{EX} differentiation trajectory, within and across T_{EX} subsets, marked by enhanced effector cytokine and granzyme B production. The more potent state remains differentially prominent in a T cell-mediated tumor clearance model, where they also show increased engagement in the microenvironment and are superior in tumor cell killing. Employing multimodal CITE-Seq in human head and neck tumors enables a similar strategy to identify Cd69RNA^{hi}CD69+ cells that also have enhanced functional features in comparison to Cd69RNA^{lo}CD69+ cells, again within and across intratumoral CD8 T cell subsets. Refining the contours of the T cell functional landscape in tumors in this way paves the way for the identification of rare exceptional effectors, with imminent relevance to cancer treatment.

43 **Introduction:**

44 Within broadly immunosuppressive tumor microenvironments (TME), pockets of rare reactive
45 immunity have been discovered, such as those containing conventional type 1 dendritic cells
46 (cDC1s) that support CD8 T cells through antigen presentation(*1-4*). T cells, which integrate their
47 encounters with antigens over their lifetime(*5-7*), require potent antigen stimulation for anti-tumor
48 function. Yet chronic stimulation by persistent antigen in the TME conversely drives precursor
49 CD8 T cells to dysfunctional or exhausted (T_{EX}) states(*8*), notably driven by TOX expression(*9,*
50 *10*). This undesirable path to T cell exhaustion is increasingly well understood including its
51 developmental stages(*11-13*), molecular markers(*10, 14-18*), transcriptional, epigenetic(*10, 15,*
52 *19-22*) and microenvironmental drivers(*23-26*). While such knowledge has been critical to shape
53 our understanding T cell dysfunction in tumors, explicit strategies to delineate potent cytotoxic
54 CD8 T cells within this exhausted milieu are not well-established.

55 Tissue-resident memory cells (T_{RM}s) expressing CD69 and/or CD103 are one possible class(*27,*
56 *28*) that might diverge from the lineage of T_{EX} differentiation and define augmented effector
57 function(*29*). While cells bearing these markers have been implicated in strong anti-tumor
58 responses(*30, 31*), the degree to which cells defined by these markers are homogeneous or
59 divergent from exhaustion are yet to be fully determined(*29, 32*). Efforts to identify potent effector
60 functions in chronic stimulation conditions have also led to identification of their $TCF1^{hi}$
61 progenitors, and the relevance of these to anti-tumor immunity is well-established, especially in
62 the context of immune checkpoint blockade(*17, 33, 34*). However, such progenitor-like CD8 T
63 cells can produce divergent trajectories of T_{EX} cells, including those biased towards effector-like
64 states(*35*).

65 Substantial previous studies have mapped T_{EX} trajectories that lead to terminally exhausted
66 T_{EX}^{Term}, notably identifying intermediates defined by KLR-expression (T_{EX}^{KLR})(*12, 13*) which in turn
67 have associated with better outcomes and cytotoxicity(*36*). Along the trajectory are also a

68 population of Ly108-CD69- intermediate Tex(*37*), derived and distinct from the progenitor subsets
69 that are Ly108+(*11*) and driven by TCF1 and MYB(*17*). These particular intermediate phenotypes
70 likely also retain some plasticity to be directed away from terminal differentiation(*12, 36, 37*).
71 Despite this well-delineated trajectory of differentiation, there is a diversity of cytotoxic potential
72 among these T_{EX} subsets, and strategies to understand the potency of effector function within
73 them are needed.

74 Evidence that effector function may not be fully dictated by the T_{EX} differentiation derives from
75 studies of key transcription factors (TF), such as suppression of progenitor-associated factors
76 TCF1(*19*) and MYB(*17*) expression, and over-expression of the AP-1 transcription factors
77 JUN(*38*) as well as STAT5A(*37*) and BATF(*39*). Downregulation of early activation gene
78 transcripts including *JUN* and *NR4A1* is a well-known response to stimulation in T and B cells(*40,*
79 *41*). AP-1 transcription factor over-expression on the other hand, counteracts the effects of TOX-
80 mediated T cell dysfunction in the context of chronic viral infections and chimeric antigen receptor-
81 expressing T cells(*37, 38*).

82 A key marker related to T cell function is the protein CD69 which has been used both to define
83 T_{RM} identity and as a marker for early activation. Prior to our study, it was understood that T cells
84 possess post-transcriptional regulatory mechanism for this 'early-response' gene which
85 dissociates its transcription (associated with AP-1(*40, 41*) and therefore likely to decrease with
86 repetitive stimulation) from its protein levels(*42, 43*). This dissociation of RNA and protein, which
87 in a broader context is well-established in T and B cells(*44, 45*), offers an opportunity to study T
88 cell states via comparisons of transcript levels related to history, separate from the CD69 protein
89 levels indicating recent activation or long-term residency.

90 Here, we report the generation of a transcriptional reporter of CD69 RNA that together with paired
91 analysis of CD69 protein, provides a novel window into the relationships between previous T cell
92 activation history and their current capacity as cytotoxic and cytokine-producing effectors. The

93 ability to mark such a dimension of effector states substantially refines the existing landscape of
94 T cell dysfunction in tumors by providing a layer of gene expression and function, beyond that of
95 the established differentiation trajectories.

96 ***Results***

97 While the cell surface expression of a protein like CD69 has historically been used to indicate
98 both T cell stimulation and tissue retention(*46*), bioinformatic analysis of multiple datasets showed
99 that the transcription of the *Cd69* gene was in fact inversely correlated with a history of chronic
100 stimulation. For example, *Cd69* mRNA itself is higher in naïve vs. effector and early progenitor
101 vs. terminally exhausted CD8 T cells **(Fig. S1a-c)**, is also higher in T cells in tumor-adjacent
102 normal areas versus those within paired colorectal cancers (CRC) tumors (associated with T_{EX})
103 (**Fig. S1d**). Further, expression of the transcription factors regulating *Cd69*(*47*) were also
104 differentially lower in exhausted vs. naïve CD8 T cells (**Fig. S1e**). In contrast, CD69 protein
105 expression, driven by TCR stimulation or other stimuli such as interferons(*48*), is often uncoupled
106 from this transcriptional activity, as a result of strong 3' UTR-mediated post-transcriptional
107 regulation(*42, 43, 49*). We thus reasoned that tracking *Cd69* RNA alongside its protein might
108 together provide a useful means to differentiate the potency of activation states in T cells.

109 ***A novel genetic tool to report T cell stimulation history in vivo*****:** To explore this idea, we
110 generated mice in which DNA encoding the teal fluorescent protein (TFP), CreER^{T2} and a polyA
111 site was inserted at the 5' end of the *Cd69* locus (hereafter referred to as *Cd69*-TFP) **(Fig. 1a)**. In
112 lymph nodes of unchallenged *Cd69*-TFP mice, the majority (~80%, **Fig. 1b**) of CD8 T cells were
113 TFP^{hi} without expressing surface CD69 protein, as measured by antibody staining (hereafter Q1
114 or TFP^{hi}CD69-). We validated that the TFP levels we measured reflected *Cd69* RNA expression
115 at steady state (**Fig. 1b, c**), and this is consistent with previous studies showing that resting T
116 cells maintain relatively high levels of *Cd69* transcript that are translationally repressed until
117 stimulation(*43, 50, 51*). In addition to this majority population, a small portion of CD8 T cells
118 expressed CD69 protein on their cell surface alongside TFP (~5%, Q2: TFP^{hi}CD69+), possibly
119 representing recently stimulated cells and a third population (~15% Q3: TFP^{lo}CD69-) was low for
120 both TFP and CD69 (**Fig. 1b**). Both TFP and CD69 protein levels rose significantly in the context

121 of robust stimulation - during the early and intermediate stages of thymic positive selection (**Fig.**
122 **S2a-d**) (*52*) as well as during the first 3-16h of stimulation of isolated peripheral CD8+ T cells with
123 anti-CD3/CD28 beads (**Fig. S2g**). CD69 protein positive cells in both of these settings, in which
124 a majority of cells are expected to be antigen inexperienced, appeared dominantly in the
125 transcript-high Q2 quadrant (**Fig. S2b, d**). We found that expression patterns for the CD69 protein
126 were similar in reporter and WT mice in both cases (**Fig. S2f, i**), although surface CD69 levels by
127 MFI were routinely about 50% lower (**Fig. S2e, h**). Difference in levels were stable when CD8 T
128 cells were sorted by TFP expression and rested in IL-7 overnight suggesting they were not reliant
129 on recent TCR stimuli (**Fig. 1d**).

130 In unchallenged mice, TFP expression in CD8 T cells varied with differentiation state, consistent
131 with Fig. S1a. Thus, $CD44^{lo}CD62L^{hi}$ naïve cells expressed higher TFP at baseline than
132 $CD44^{hi}CD62L^{lo}$ effector CD8 T cells (**Fig. 1e)**. $CD44^{hi}CD62L^{hi}$ central memory T cells (memory)
133 demonstrated higher levels still, which may be related to higher AP-1 transcription factor
134 activity(*53*) . $CD44^{lo}CD62L^{lo}$ cells expressed the lowest average level of TFP among the
135 populations. When TFP^{hi} memory and TFP^{lo} effectors were sorted from spleens of unchallenged
136 mice and stimulated with anti-CD3/anti-CD28 beads for 3h, TFP^{hi} cells generated more CD69
137 surface protein as compared to TFP^{lo} cells, an effect also observed in the presence of Actinomycin
138 D treatment to block new transcription (**Fig. 1f, g**). Both groups maintained their pre-existing TFP
139 status during this short stimulation, demonstrating how T cells occupying the Q4:$TFP^{lo}CD69+$
140 cells may be generated from Q3:$TFP^{lo}CD69-$ cells (**Fig. 1f**). Finally, we found that the Q4:
141 $TFP^{lo}CD69+$ quadrant was modestly represented in skin-resident CD44+CD103+ CD8 T_{RM}s from
142 6 mo. old mice (**Fig. 1h, j**) and dominant in ovalbumin-specific OT-I T cells in the spontaneous
143 mammary tumors in genetically modified PyMTchOVA mice (*54*) 12d after adoptive transfer (**Fig.**
144 **1i, j**). The opposite was true for the Q2: $TFP^{hi}CD69+$ quadrant (higher in T_{RM} than tumor) (**Fig.**

145 **1h-j**). Together with our informatic data, this supported the association between TFP levels and
146 a history of encounters in CD8 T cells.

147

148 To further explore this possible relationship of TFP^{lo} cells with a history of repeated stimulation,
149 we set up repetitive "chronic" stimulation cultures using purified CD8 T cells from *Cd69*-TFP mice.
150 Cells were subjected to 3 cycles of 48h stimulation with 1:1 anti-CD3/anti-CD28 beads, followed
151 by 72h rest under either hypoxia (1.5% O_2) or ambient oxygen levels (normoxia), in the presence
152 of low concentrations of IL-2 after the first cycle (**Fig. 2a, Fig. S3a**). The hypoxic condition has
153 been shown previously to augment the acquisition of exhaustion-like features (*55*). *Cd69*-driven
154 TFP levels at the end of each cycle were lower than the previous, an effect that culminated in
155 about a 50% and 30% reduction under hypoxia and normoxia after 3 cycles, respectively (**Fig 2a-**
156 **c, Fig. S3a, b**). Repeated stimulation concurrently upregulated exhaustion-associated markers
157 such as PD1, CD38 and Tim-3, accentuated under hypoxia(*55*) (**Fig. 2f, Fig. S3d, e**). Addition of
158 IL-2 without TCR stimulation (**Fig. S3f**) did not induce differentiation (**Fig. S3g**), decline in TFP
159 expression (**Fig S3h**), nor acquisition of exhaustion-associated markers (**Fig. S3i**). While both
160 *Cd69* mRNA (**Fig. 2d, Fig. S3c**) as well as the upstream AP-1 transcription factor *Jun* (**Fig. 2e**)
161 decreased with repeated stimulation, a faster initial decay was observed when compared to the
162 TFP reporter, likely due to longer half-life of TFP.

163 Analyzing the 24h time point in each cycle indicated a progressively lower magnitude of reporter
164 expression by MFI, from Cycle 1 to Cycle 3 (**Fig. S3j**), which contrasted with effector differentiation
165 and activation marker CD44, whose peak levels increased in every cycle (**Fig. 2a, Fig. S3a**).
166 However, by the time we sampled 24h post stimulation, we noticed that %TFP^{hi} had reverted to
167 ~100% in each cycle (**Fig. 2a**). To test whether TFP levels after a shorter stimulation length is
168 dependent on the history (cycle number), we further sampled stimulated cells at each cycle at 3,
169 6 and 18h time points (**Fig. 2g**). Indeed, both in terms of MFI as well as %TFP^{hi}, we observed

170 significantly and progressively lower levels of TFP expression at these intermediate time points
171 (**Fig. 2g**). Therefore, to reach the same levels of TFP more stimulation is necessary in later cycles,
172 demonstrating the inherent hysteresis and dampening in the system.

173 To test whether low TFP levels implicated different functionality, we sorted TFP^{hi} vs. TFP^{lo} cells
174 from 'Cycle3 0h' and assayed cytokine and GzmB production after overnight (16h)
175 PMA/ionomycin stimulation. This revealed that a higher proportion of TFP^{hi} cells and co-
176 expressed TNF-α and IFN-γ and tended to be positive for GzmB compared to TFP^{lo} counterparts
177 (**Fig. 2h**). A net model based on this set of experiments (**Fig. 2i**) proposes that in RNA
178 (CD69:TFP) space, trajectories of CD8 T cell state are not retraced during subsequent activation
179 events—rather, TFP levels decrease with repeated stimulation. Further, these in vitro experiments
180 suggest that TFP^{hi}CD69+ Q2 cells in this reporter system—displaying increased effector
181 functions—are ones that are recently activated yet have not been subject to chronic and
182 exhaustive stimulation.

183 **Delineation of chronic vs. potent activation states in tumors:** To study this reporter in the
184 context of *in vivo* tumor biology, we adoptively transferred *Cd69*-TFP reporter positive ovalbumin-
185 specific CD8 T cells from CD45.1; OT-I TCR transgenic mice into WT mice bearing
186 subcutaneously injected B78chOVA (OVA and mCherry expressed in B78, which is an amelanotic
187 variant of B16F10 melanoma (*23*)) tumors (**Fig. 3a**). B78 is a an amelanotic B16 variant, which
188 we have previously described as un-responsive to OT-I treatment and where adopted T cells are
189 progressively rendered dysfunctional in the tumor(*23*). Recovered OT-Is from these tumors, were
190 ~90% PD1+ CD44+ (**Fig. S4a**) and were largely found in Q1 and Q2 of the reporter system on
191 the first day they were detected (day 4)**,** with endogenous intratumoral CD8 T cells used as the
192 internal control to set the TFP gate (**Fig. 3b)**. While we found low levels of CD69+ among recently
193 arrived T cells, consistent with the required loss of CD69 expression to emigrate from the dLN(*56*),
194 by day 6-7 ~70% of cells were $TFP^{hi}CD69^{+}$ (Q2: **Fig. 3b, d)**. By day 14, recovered cells were

195 dominantly TFP^{lo}CD69^{-} (Q3) and TFP^{lo}CD69^{+} (Q4) (**Fig. 3b, d).** Consistent with our previous work
196 using this(*23*) and other models(*54*), this shift to TFP^{lo} states was accompanied with increased
197 differentiation towards chronic stimulation-driven exhaustion, here measured by PD1+CD38+(*15,*
198 *23*) among OT-Is (**Fig. S4b**), which also tracked with TOX^{hi}TCF7^{lo} phenotypes (**Fig. S4c**). Similar
199 trends in intratumoral OT-Is were observed in a spontaneous breast carcinoma tumor model
200 (PyMTchOVA)(*54*) with adoptive transfer, albeit with a less prominent transient increase in Q2
201 (**Fig. S4d-f**).

202 An alternative hypothesis to attributing these changes to differentiation is one in which cells
203 migrating from the lymph node were progressively decreasing in TFP levels and replacing those
204 in the TME. When the draining lymph node (dLN) was analyzed, in contrast to the tumor, we found
205 the vast majority of cells remaining TFP^{hi} throughout the experiment. (**Fig. 3c, e**) suggesting that
206 the observed changes more likely relied on features of the tumor microenvironment. As another
207 way to address the competing hypothesis more directly, we modified a tumor slice overlay
208 protocol(*57*) to create an experiment in which a selection of T cells encounter the TME at the
209 same time with no further migration being possible (**Fig. 3f**). In this setting, the progression of
210 phenotypes through CD69:TFP quadrants (**Fig. 3g, Fig. S5a)** and the acquisition of exhaustion
211 markers (**Fig. S5b-d**) recapitulated what we had seen in vivo, suggesting that encounter with the
212 tumor microenvironment (TME) was sufficient to drive these changes. Slice cultures also allowed
213 analysis of proliferation in the slice-infiltrating OT-I T cells over time using violet proliferation dye
214 (VPD) (**Fig. S5e**). VPD dilution accompanied the general decrease in TFP expression with each
215 division, exemplified at day 3 **(Fig. S5f**). Q4 cells at d8 had undergone more division (**Fig. S5g**)
216 and were significantly more PD1^{+}CD38^{+} than those from Q2 (**Fig. S5h**), suggesting that they were
217 further along the T_{EX} differentiation trajectory. In fact, analyzing the level of VPD within cells in the
218 four CD69:TFP quadrants at each time point reinforced the trajectory of transition from TFP^{hi} Q1
219 and Q2 states to TFP^{lo} Q3 and Q4 states (**Fig. S5i**).

220 To further assess the conversion of T cells among these CD69:TFP states in the context of
221 tumors, we sorted OT-Is d12 post transfer by their CD69:TFP phenotypes from B78chOVA tumors
222 (Q2-Q4) and the dLN (Q1), restimulated these cells in vitro with anti-CD3/CD28 beads, and
223 tracked the resultant quadrant transitions after 3d (**Fig. 3h, i**). Q1 cells transitioned to Q1 and Q2
224 and partially to Q3, while Q2 converted to Q2 and Q4, with small percentages in Q1 and Q3 (**Fig.**
225 **3h, i**). Sorted Q3 and Q4 cells both remained predominantly (~70-80%) within the Q3 and Q4
226 states – suggesting a propensity to inter-convert between these states (**Fig. 3h, i**). Of note, both
227 Q3 and Q4 cells retained some ability to convert to TFP^{hi} Q2 upon strong stimulation, although
228 this propensity was significantly lower than those of Q1 and Q2 cells (**Fig. 3h, i**). Together, these
229 data reveal a dominant trajectory of conversion from TFP^{hi} to TFP^{lo} states in tumors, consistent
230 with T cells undergoing repeated TCR stimulation.

231 To further determine how this progression from TFP^{hi} to TFP^{lo} states is related to antigen
232 stimulation and the corresponding microenvironment, we isolated CD8 T cells with a non-tumoral
233 specificity (LCMV-specific P14; *Cd69*TFP) and assessed their state both within a tumor that did
234 not express their antigen or from within a vaccination site, as compared to OT-I T cells from an
235 OVA-expressing tumor (**Fig 3j**). When the P14; *Cd69*TFP cells were co-injected with CD45.1; OT-
236 I; *Cd69*TFP T cells into B78chOVA tumor-bearing mice, that then received a priming gp33-41
237 peptide vaccination distal to the tumor (**Fig. 3j**), we found that they expressed higher TFP levels
238 in the tumor than OT-Is (**Fig. 3k, l**). P14 T cells at the contralateral vaccination site also remained
239 substantially TFP^{hi} with a 5x increase in the frequency of cells Q2 (**Fig. 3k, l**) than tumor OT-Is.
240 These differences in CD69:TFP quadrant distributions aligned with the expression of surface
241 markers PD1, CD38 and CD39, associated with exhaustion (**Fig. 3m**). Overall, these surface
242 proteins were highest in the intratumoral OT-Is, intermediate in the P14s at the vaccination site
243 and comparatively low in the non-specific intratumoral P14s (**Fig. 3m**). Hence, exposure to the
244 TME alone did not lead to loss of a Q2 state, and presentation of antigen at a different site also

245 did not lead to decreases in TFP level. Overall, these data support that antigen-specific
246 stimulation of T cells specifically in a TME can drive a CD69+TFP^{lo} (Q4**)** phenotype.

247

248 **TFP^{hi}CD69+ Q2 marks a state of relative functional potency in T_{EX} cells:** We next sought to
249 establish whether Q4 and Q2 cells were also functionally different in tumors and determine how
250 this related to T_{EX} cell differentiation in tumors, best highlighted in single-cell sequencing(*12, 58,*
251 *59*). We thus pooled OTI; *Cd69* TFP T cells from eight B78chOVA tumors 12d after adoptive
252 transfer and sorted for CD69:TFP quadrants, barcoded each population separately and performed
253 single cell RNA Sequencing (scSeq) (**Fig. 4a**). From 13,352 cells, nine computationally derived
254 clusters were identified (**Fig. Fig. 4b**), driven largely by the same canonical markers of previous
255 works and with similar predicted differentiation trajectories (**Fig. S6a- c**). Strong associations were
256 observed between the gene expression patterns corresponding to Tex^{Prog}, Tex$^{E.Eff}$, Tex^{Term}, Tex^{ISG}
257 and Tex^{KLR} subsets in our dataset and those that previously established this nomenclature(*12*)
258 (**Fig. S6e**). This is consistent with the use of the same nomenclature in this context, although
259 some differences exist such as in the $T_{EX}^{Int.}$ and T_{EX}^{Mem} subsets – and may be attributable to
260 variability between tumor and LCMV-derived subsets in those other works.

261 Barcoding of sorted cells by CD69:TFP states then allowed us to map quadrant distributions of
262 these post-exhaustion T cell subsets (T_{EX})(*12*), (**Fig. 4b, c, Fig. S6d**). In agreement with the
263 evolution of CD69:TFP quadrant distributions in Fig. 3, T_{EX}^{Prog} cells were barcoded as coming
264 from to Q1 or Q2 states and more terminally differentiated subsets of T_{EX}^{Int}, T_{EX}^{Term} were
265 dominantly derived from Q3 and Q4 barcoded cells (**Fig. 4c**). $T_{EX}^{KLR\ Eff}$, previously the most likely
266 candidates to have high effector function, were heterogenous, expressing barcodes indicative of
267 either Q2 or Q4.

268 Using flow cytometry to mark the differentiation trajectory similarly, we found that Progenitor
269 (TCF1+) were dominantly associated with Q1 and Q2, putative 'effectors' (CD94+: CD94 or
270 KLRD1 is the gene product of *Klrd1,* one of the markers of the $T_{EX}^{KLR\ Eff}$ subset) dominantly were
271 Q2 and Q4 (with Q2>Q4) and 'exhausted' (PD1+CD38+) cells were enriched in Q4 and Q2
272 (Q4>Q2) (**Fig. 4d-f**), trends also recapitulated in spontaneous mammary PyMTChOVA tumors
273 (**Fig. S7a-c**). The distribution of important transcription factor and other canonical marker
274 expression also supported this broad relationship between T cell differentiation and CD69:TFP
275 distributions (**Fig. 4g**). Transcripts for progenitor markers primarily concentrated in Q1, AP-1
276 factors in Q1 and Q2, while exhaustion-related markers largely occupied Q3 and Q4 states.
277 Effector lineage and function-associated *Batf* and *Tbx21, Ifng* were highest in Q2 (Q2>Q4), along
278 with signatures of non-canonical enhanced effectors derived from STAT5A overexpression(*37*)
279 or MYB KO(*17*) (**Fig. 4g**). T_{RM} markers(*28*) *Prdm1,* and *Id2* tended to be higher in TFP^{lo} Q4 than
280 TFP^{hi} Q2 in this context (**Fig. 4g**). A core tissue residency signature (*60*) also appeared split
281 between Q2 and Q4 (Q2 > Q4) (**Fig. S6f**), while an orthogonal circulatory gene signature(*60*) was
282 concentrated in Q1 and Q2 (**Fig. S6f**) – consistent with the early arrivals and those in the dLN
283 being TFP^{hi}. Identifying T_{RM}-like cells by CD103 and CD69 expression by flow cytometry, we found
284 their relative abundances in the Q2 and Q4 states to be similar (**Fig. S6g**), although the frequency
285 of such cells among intratumoral OT-Is in this relatively short time of residence was only around
286 1% on average (**Fig. S6h**). A gene signature associated with transitory checkpoint blockade
287 associated CD101-Tim3+ effectors were highest in Q2 and that of its CD101+Tim3+ terminally
288 exhausted counterpart (*13*) was highest in Q4 followed by Q3 (**Fig. 4g**).

289 Within the entire population we found enhanced expression of intracellular cytokines TNF-α, IFN-
290 γ and cytotoxicity-associated GzmB in intratumoral Q2 cells as compared to their Q4 counterparts,
291 with restimulation post-sorting (**Fig. 4h-i, Fig. S7d**) as well as at baseline (**Fig. 4j, Fig. S7f, g**).
292 Notably, Q1 cells were comparably cytokine and granzyme positive upon restimulation as Q2,

293 while Q3 cells were similarly low response as Q4 (**Fig. 4i, Fig. S7d**). Without restimulation, Q2
294 cells were significantly more cytokine and granzyme producing that Q1 and the same was true
295 for Q4 and Q3 (**Fig. S7e**), suggesting the conversion of re-activated cells from Q1 and Q3 to Q2
296 and Q4 respectively. The observation that effector-like and exhausted cells (delineated in single-
297 cell transcriptomes and flow cytometry) both showed evidence of Q2 cells (**Fig. 4c, Fig. S6d**)
298 implied the possibility that those demarcations may not fully capture the effector function potential
299 of these cells. We thus interrogated Q2, as compared to Q4 cells from distinct differentiation states
300 to determine whether there were variations in functional potency within each given classification.
301 We gated further on subsets that were split between the Q2 and Q4 state – namely an early
302 progenitor Ly108+CD69+(*11*) (56% Q2 and 44% Q4: **Fig. 4k**), an effector-like CD94+ (33% Q2
303 and 46% Q4: **Fig. 4l**) and terminal exhaustion-like PD1+CD38+ (23% Q2 and 53% Q4: **Fig. 4m**)
304 subset, appearing at different junctures of the T_{EX} differentiation trajectory. Within Ly108+CD69+
305 (**Fig. 4k**) subset, cells in the Q2 state were higher than those in Q4 in TNF-α and IFN-γ (but not
306 GzmB). Of note, a second progenitor population Ly108+CD69- (*11*), split between Q1 and Q3
307 showed lower cytokine and granzyme levels overall than Ly108+CD69+ and no significant
308 difference between Q1 and Q3 (**Fig. S7h**). Further, within CD94+ (**Fig. 4l**) and PD1+CD38+
309 subsets as well (**Fig. 4m**), cells in the Q2 state consistently showed higher expression of these
310 cytotoxic molecules in most cases than the Q4 counterparts (only TNF-α within CD94+ was not
311 significantly different). The Ly108-CD69+ terminal subset aligned with the latter (PD1+CD38+)
312 subset (~83% of Ly108-CD69+ cells were PD1+CD38+: **Fig. S7i**), consistent with their
313 association to terminal exhaustion, and therefore demonstrated similar Q2 vs. Q4 differences in
314 cytokine and granzyme expression (**Fig. S7j**). Thus, this delineation of *Cd69* transcription (by
315 TFP) among CD69+ cells provides an additional layer indicative of relative functionality of CD8 T
316 cells over and above the established trajectory of an intratumoral T_{EX} differentiation landscape.

317

318 **Evidence of enhanced Q2 (TFP^{hi}CD69^{+}) CD8 T cell function during tumor regression:** We
319 next tested whether CD8 T cells in this activation state Q2 would be more prominent during a
320 productive anti-tumor response such as T cell-mediated tumor control. To do this, we investigated
321 subcutaneously injected MC38chOVA (MC38 colorectal cancer cell line modified with the same
322 chOVA construct as PyMTchOVA (*54*) and B78chOVA) tumors that are actively controlled in
323 response to the adoptive transfer of ovalbumin-specific OT-I T cells, whereas B78chOVA are not
324 (**Fig. 5a**). We found that *Cd69*-TFP;OT-I T cells in regressing MC38chOVA tumors retain their
325 predominantly Q2 (CD69^{+}TFP^{hi}) phenotype even at d12 post adoptive transfer, in contrast to
326 those in the growing B78chOVA tumors (**Fig. 5b, Fig. S8a**). Conversely, the chronic activation-
327 induced Q4 (CD69+TFP^{lo}) subset was significantly lower in MC38chOVA compared to B78chOVA
328 (**Fig. 5b**). However, the relatively high TFP^{hi} proportion (at least 60% at all time points) in the
329 corresponding dLNs was similar in both (MC38chOVA :**Fig. S8b,** B78chOVA : **Fig. 2c, d**).

330 From d5 to d12, transferred OT-Is in MC38chOVA tumors showed a decline in Ly108 expression,
331 and a concomitant increase in exhaustion-associated co-expression of PD1 and CD38, although
332 the percentage of the latter was lower than that in B78chOVA (**Fig. S8c:** MC38hOVA**, Fig. S4b**:
333 B78chOVA). Further investigation revealed the OT-I cells in the MC38chOVA tumors were ~80%
334 CD94 (KLRD1)+ at d5, which rose to be >90% at d12 (**Fig. S8c**). This was significantly higher
335 compared to about 25% in the B78chOVA model (**Fig. 5c, d**), indicating a dominant KLR-effector
336 phenotype in the MC38chOVA(*36*). Once again, the CD103+ subset of the transferred OT-Is was
337 only around 1% (**Fig. S8c**), therefore ruling out T_{RM}-like cells as the dominant potent effectors in
338 this context. Among these largely KLRD1+ OT-I T cells in MC38chOVA, those in the Q2 state
339 again tended to express markedly higher levels of TNF-α and IFN-γ and GzmB than Q4
340 counterparts, consistent with B78chOVA (**Fig. 5e-g**). These trends were already prevalent at d5
341 and showed a stronger divergence of phenotypes at d12 (**Fig. 5g**). Further evidence of in situ
342 functional engagement of TFP^{hi} cells was obtained by two-photon microscopy where those cells

343 could be identified by analysis of TFP levels over non-TFP controls (**Fig. S8d**). This analysis
344 demonstrated enhanced cell arrest of the TFP^{hi} (majorly ~75% Q2) cells within MC38chOVA
345 tumor slices harboring adopted OT-Is, with lower speed (**Fig. 5h, i**), directional persistence (**Fig.**
346 **5j**), and overall motility (**Fig. S8e)**. In both mouse(*61*) and human(*57*) tumors, these traits are
347 associated with lower levels of exhaustion. In addition, among the OT-I cells sorted from
348 MC38chOVA tumors by CD69:TFP quadrants, those in the Q2 state also showed the highest
349 killing capacity when exposed to MC38chOVA cells in vitro (**Fig. 5k**). These data substantiate the
350 use of TFP and CD69 to mark a potent activation state of intratumoral CD8 T cells in mice.

351

352 **Demarcation of *Cd69* RNA levels enables functional delineation of CD69+ CD8 T cells**
353 **across exhausted T cell subsets in human head and neck tumors:** We next sought to
354 independently identify similar CD8 T cell activation states in human tumors**,** now using multimodal
355 CITE-Seq on Head and Neck Squamous Cell Carcinoma (HNSC) tumor biopsies (**Fig. 6a**). Within
356 tumor-derived cell populations, we gated on CD8 T cells using antibody-tagged markers (**Fig.**
357 **S9a**), and simultaneous readouts of Cd69 mRNA and surface CD69 protein expression allowed
358 CD8 T cells to be gated into 4 quadrants (akin to Cd69-TFP reporter mice) (**Fig. S9b)**. Unbiased
359 combined protein-RNA driven weighted nearest neighbor determination differentiated CD8 T cells
360 into 7 major clusters and 2 minor, atypical clusters (MT+ and CXCL2+) (**Fig. 6b**). Based on the
361 DEGs and overlaying exhaustion and naïve markers that were detected at the surface protein
362 level by antibody-derived tags (**Fig. 6c**), we identified a naïve (Tn), a memory (Tem) and 5
363 exhaustion-associated clusters, including a proliferative and a CXCL13-expressing subset (**Fig.**
364 **6b, S9c, d**). In contrast to the Naïve and exhaustion scores, expression of progenitor and effector
365 gene expression previously identified in chronic infection in mice(*12*) revealed diffuse expression
366 in the major clusters (**Fig. S9e**). This may be expected since the trajectory of differentiation and
367 typical subset identities in such human tumors are not identical to the T_{EX}-differentiation

368 trajectories in mice. Therefore, we used scSeq data corresponding to a recently published pan-
369 cancer CD8 T cell atlas(*62*) and overlaid the DEGs for each major cluster in our dataset onto the
370 established nomenclatures in the published atlas (**Fig. S9f, g**). This analysis supported the
371 classification of the five exhausted (Tex) clusters as 'early', intermediate or 'int', 'late', cycling or
372 'cyc' and 'CXCL13', while Tn and Tem signatures corresponded directly to naïve and memory
373 clusters in the atlas (**Fig. S9g**). Among the Tex clusters, the Tex^{Early} closely resembled TCF1+
374 Tex and OXPHOS- Tex from the atlas, the Tex^{Int} bore mild similarities to one NK-like Tex cluster,
375 while Tex^{Late} and Tex^{CXCL13} were similar to Terminal Tex cluster in the atlas, which also expressed
376 *CXCL13* (**Fig. S9c, g**). As in mice, Q2 ($Cd69RNA^{hi}CD69Protein^{+}$) and Q4
377 ($Cd69RNA^{lo}CD69Protein^{+}$) states in this human tumor sample also spanned several clusters (**Fig.**
378 **6d**). A majority of the exhausted CD8 T cells existed in the Q4 state, as indicated by the
379 coincidence of the exhaustion score (based on protein expression) and the Q4 cells (**Fig. 6c, d**).
380 Representation of the Q2 state was skewed towards the Tn, Tem and Tex^{Early} and that of Q4
381 towards the Tex^{Late} , Tex^{CXCL13} subsets and the Tex^{Int} cluster (**Fig. 6e**).

382 Having classified both the Tex subsets and the Q1-Q4 quadrants within these intratumoral CD8
383 T cells, we then investigated the patterns of functional gene expression between the Q2 and Q4
384 states. Using the CITE-Seq data in a patient-by-patient analysis (**Fig. S9h**), we found that Q2
385 cells expressed significantly higher levels of AP-1 transcription factors *JUN* and *FOS* (STAT5A
386 was poorly represented in this dataset) with 7 head and neck cancer patients as biological
387 replicates (**Fig. 6f**). Enhanced expression of *IFNG* as well as a decreased Exhaustion score
388 (calculated from antibody tags to exhaustion-related surface proteins) in Q2 as opposed to Q4
389 cells (**Fig. 6g**) indicated similar, functionally divergent activation states, as those elucidated in
390 mice. Notably, as with the murine scSeq data, T_{RM}-like cells delineated by CD103 protein
391 expression were represented both in Q2 and Q4 states (**Fig. S9i**). We next interrogated whether
392 the features of this delineation remained true within different subsets of cells, by delving into the

393 individual Tex^{Early} and Tex^{Late} subsets, with sufficient representation (using a threshold of 50 cells
394 in a given sub-group for obtaining reliable gene signature scores) in 3 and 4 patients respectively
395 as biological replicates. Even within these distinct Tex subsets, the same trends of enhanced *JUN*
396 and *IFNG* expression and decreased Exhaustion (only Exhaustion in Tex^{Early} remained indifferent)
397 were observed (**Fig. 6g**), indicating a similar axis of effector function over and above the Tex
398 differentiation trajectory.

399

400 **Delineation of potent effector states across human cancers:** To the extent that transcriptomic
401 signatures can capture the multimodal delineation offered by our reporter and then by CITE-Seq,
402 these are useful in their imminent applicability to the already existing transcriptomic data on
403 human tumors. With this objective, we obtained DEGs between Q2 and Q4 states from CITE-
404 Seq. The Q2 signature included not only *CD69,* but also its upstream transcription factors *JUN,*
405 *FOS* and *NR4A1*, while the Q4 signature largely comprised of actin-related genes and *CD74* (**Fig.**
406 **7a**). We then overlaid the expression of the gene signatures for Q2 and Q4 onto the pan-cancer
407 CD8 T cell atlas described above(*62*) (**Fig. 7b**). We arranged the well-represented and
408 characterized clusters (therefore excluding Tc17 (IL-17-related) and the NME-1+ clusters) in
409 decreasing order of the naïve gene expression score (*SELL, IL7R, TCF7, LEF1, CCR7*) (**Fig. 7c**).
410 As expected, the exhaustion gene expression score (gene list as previously described(*63*)) in the
411 same clusters displayed approximately the opposite (increasing) order (**Fig. 7c**). Notably, while
412 the Q4 score tended to coincide in pattern of expression with the exhaustion score, the Q2 score
413 was distinct from both Naïve and Exhaustion score expressions (**Fig. 7c**). The Q2 score was
414 prominent in the intermediate NK-like CD8 T cells expressing effector markers, while the Q4
415 signature associated highly with *GZMK* and *CXCL13* expressing T_{EX} subsets, which appear later
416 in the predicted differentiation towards exhaustion (**Fig. 7c**).

417 As with the mouse scSeq, in this analysis of human tumor-infiltrated CD8 T cells, we further
418 included previously identified exhausted T cell subsets in addition to our Cd69 RNA-based
419 delineations. Specifically, transcriptomic signatures reported for phenotypically opposing
420 Ly108+CD69+ vs. Ly108-CD69+(*11*), and CD101-Tim3+ vs. CD101+Tim3+ subsets(*13*) using
421 human ortholog genes were examined. Cell-by-cell expression of Ly108-CD69+ and
422 CD101+Tim3+ signatures (both of which are associated with terminal exhaustion) moderately
423 correlated with each other (rho = 0.48) (**Fig. S10c**). The Q4 signature showed weaker (rho = 0.27,
424 0.25) correlation with both aforementioned signatures, while Q2 was largely uncorrelated with all
425 other signatures (**Fig. S10c**). Notably these pairs of gene signatures (Q2 vs. Q4, Ly108+CD69+
426 vs. Ly108-CD69+ and CD101-Tim3+ vs. CD101+Tim3+ subsets) were not negatively correlated
427 with their counterparts (**Fig. S10c**). Therefore, we gated on cells based on the ratio of Q2/Q4
428 signature scores within three distinct subsets - Gzmk+ early Tem, ZNF683+ T_{RM} and Terminal
429 Tex - to test whether the Q2 and Q4 states represented divergent functional states within and
430 across these subsets. Overall, the Q2/Q4 ratio^{HIGH} cells showed higher expression of effector
431 cytokine transcripts *IFNG, TNF* and lower Exhaustion as compared to the Q2/Q4 ratio^{LOW} cells
432 within these subsets, although the extent of these differences varied (**Fig. 7d-f**). In contrast, cells
433 gated on the value of Ly108+CD69+/Ly108-CD69+ signature ratio were more often indifferent or
434 skewed in the opposite direction with respect to the same metrics (**Fig. S10a**). The CD101-
435 Tim3/CD101+Tim3+ ratio, while more variable showed some similarities with the trends in the
436 Q2/Q4 delineation (**Fig. S10b**).

437 To interrogate how these Q2 and Q4 states associate with anti-tumor function in human tumors,
438 we next used these gene signatures to query patient outcome data. We stratified HNSC patients
439 from the cancer genome atlas (TCGA) using the same Q2 and Q4 signatures generated from
440 HNSC CITE-Seq, into the top and bottom 30% based on the expression of the ratio of Q2/Q4
441 signature scores. HNSC patients with gene expression patterns skewed towards the Q2, as

442 opposed to the Q4 state showed significantly better overall survival (**Fig. 7j**). In fact, patients
443 scoring high on the Q2/Q4 ratio score showed significantly better overall survival in all indications
444 combined (**Fig. 7g**). In contrast, the Ly108+CD69+/Ly108-CD69+ signature ratio was indifferent
445 to (**Fig. 7h**) and the CD101-Tim3/CD101+Tim3+ ratio correlated negatively (**Fig. 7i**) with patient
446 survival in the same TCGA cohort. While these results do not diminish the value of these
447 previously described subsets for mapping T cell exhaustion, and indeed those signatures may be
448 confounded by the presence of other cell types in their application to bulk TCGA RNAseq data,
449 they do support the Cd69 RNA-based delineation as a distinct additional categorization of
450 biological and clinical relevance.

451 By indication, in addition to HNSC, Q2/Q4 ratio was a significant survival prognostic in multiple
452 indications including Hepatocellular (LIHC), Melanoma (SKCM), Kidney (KIRC) and Lung (LUAD)
453 cancers (**Fig. 7k, l**), and in other indications (Bladder BLCA, Colorectal COAD, Glioblastoma
454 GBM, Gynecological GYN, Pancreatic PAAD, and Sarcoma SRC) remained neutral to overall
455 survival (**Fig. S10d, e**). To confirm that this association with survival was T cell-dependent, we
456 next used a smaller bulk RNA-Seq dataset from sorted intratumoral conventional T cells that was
457 part of a recent pan-cancer census(*63*). We applied the same strategy of stratifying patients (split
458 at the median here to maximize number of samples) based on the Q2/Q4 ratio. Combining the
459 above-mentioned indications (LIHC, SKCM, KIRC, LUAD, HNSC) where Q2/Q4 was associated
460 with increased survival in TCGA, we found a clear trend towards a similar association even in this
461 smaller dataset (~80 patients/group) (**Fig. 7m**). Also consistent with the TCGA analysis, in this
462 pan-cancer cohort, T cell specific Q2/Q4 ratio remained neutral to overall survival in other
463 indications (BLCA, COAD, GBM, GYN, PAAD, SRC) combined (**Fig. S10f**). While these distinct
464 outcome cohorts may be attributed to the heterogeneity across cancer types and potentially
465 distinct underlying rate-determining steps for anti-tumor immunity, it is notable that in none of the
466 indications this ratio emerges as a negative prognostic. Together, these data show that this

467 delineation of CD69+ CD8 T cells by Cd69 RNA into potent and dysfunctional activation states is
468 functionally relevant in many human cancers. Delineating this axis of potent effector states by
469 tracking *Cd69* RNA provides an additional dimension to map the contours of the exhaustion-
470 dominated T cell functional landscape in tumors.

471

472 **Discussion:**

473 In summary, we have defined a multimodal approach using transcript and protein levels of CD69
474 simultaneously to find potent effector CD8 T cell states over and above the exhausted T cell
475 lineage in tumors. Our data suggests that such states may be naturally prominent in certain tumor
476 microenvironments (MC38), and rare in others (B78/B16), with functional consequences. By
477 determining functional states associated with patterns of *Cd69* RNA and protein expression, our
478 data lend further relevance and context to the discordance between this transcript and its protein
479 expression in T cells(*42, 43*). This agrees with the distinct kinetics of transcripts and proteins
480 associated with many genes in the T and B cell repertoire (*44, 45*). Associated with tissue
481 retention(*46, 56*) or stimulation in general, the relationship between CD69 protein expression and
482 intratumoral T cell function is ambiguous. In contrast, we show that higher expression of *Cd69*
483 RNA indicates a poised or potent activation state and therefore indicative of enhanced functional
484 potential. The systematic use of *Cd69* transcription, along with its surface protein expression may
485 be similarly applicable in other important contexts including vaccination, resident memory
486 formation and autoimmunity, to directly identify and study potent activation states of lymphocytes
487 in situ. While the fast maturation time of monomeric TFP allows concordant recording of new
488 transcription, the longer half-life of the fluorescent protein makes it insensitive to rapid changes
489 as a reporter. Rather, the decline in TFP expression should be thought of as a delayed reporting
490 of decreasing transcription integrated over a period of days. Further, transcription and detectable
491 transcript levels may also be different in some conditions where mRNA degradation(*43*) rather
492 than translational repression dominates the post-transcriptional regulation. In this context, further
493 studies using the inducible Cre in the reporter construct to lineage trace activated cell states
494 marked by the reporter may be leveraged to further understand the nuance of this biology. Such
495 timed Cre-mediated conversions may further allow marking of potent effector T cells for imaging
496 as well as specific depletion in future studies.

497 Our results demonstrate that among CD69+ activated CD8 T cells, those with higher *Cd69*
498 transcription, and associated higher levels of AP-1 transcription factor expression, are functionally
499 distinct from those with lower levels of these transcripts. These data are consistent with separate
500 previous reports showing the overexpression of AP-1 factors JUN, STAT5A and BATF in CD8 T
501 cells leading to enhanced functional capacities(*37, 38*),(*39*). In the presence of AP-1 factors and
502 NFAT, BATF can promote potent effector function and counteract exhaustion(*39*) – our data
503 indicates that by the indirect recording of AP-1, NFAT activity by Cd69 transcription, this
504 strategy illuminates those cells in which such functional signaling is active.

505 Accumulating evidence suggests that exhausted CD8 T cells in the TME continue to receive sub-
506 optimal TCR stimulation, keeping them locked in a dysfunctional activation state(*21, 64*). Within
507 and across broadly defined subsets, the delineation of activation states here serves to further
508 refine our understanding of the anti-tumor potential of intratumoral CD8 T cells. Our data supports
509 the delineation of Q2 ($RNA^{hi}Protein^{+}$) and Q4 ($RNA^{lo}Protein^{+}$) as 'potent' and 'chronic' activation
510 states respectively. Q1 ($RNA^{hi}Protein^{-}$) on the other hand represents a 'poised' state, while Q3
511 ($RNA^{lo}Protein^{-}$) is a quiescent state encompassing both certain naïve and bystander cells, as well
512 as inactive exhausted cells. In this way, these results should be understood to not be 'in place of'
513 but 'in addition to' the already existing mapping of exhausted T cell states which we have
514 extensively referenced and drawn from in this work. The application of this methodology in the
515 CITE-Seq context demonstrates the potential to find functionally relevant activation states in
516 human cancers. As such, the gene signatures for the divergent activation states derived from
517 head and neck tumors may be further refined to be robust across species and indications –
518 perhaps with the aid of bulk RNA-Seq or ATAC-Seq modalities, which may offer a deeper look
519 into such states.

520 The use of CD69 protein as a primary marker of specific T cell states is a point of consideration
521 for future studies. Our data show that repetitive TCR stimulation and exposure to antigen-bearing
522 TME are sufficient for the drop in relative transcription levels and TFP and the resultant functional
523 differences between TFP^{hi} and TFP^{lo} subsets. However, given other stimuli that can induce CD69
524 expression, it is not necessary that Q2 and Q4 cells be produced by TCR-dependent
525 mechanisms. It remains to be explored whether other forms of repetitive stimulation, or
526 successive recall (in the case of memory cells) can drive such a feedback response associated
527 with decreasing function. Overall, the interpretation of CD69 protein expression likely depends on
528 these additional measures of feedback, such as its transcript levels which are shown here to be
529 related to history and effector function.

530 Successful boosting of anti-tumor immunity in rare pockets of reactive immunity(*1, 65, 66*) may
531 lead to the generation of stronger effector CD8 T cells, inducing functional features within subsets
532 of exhausted T cells, perhaps without entirely reversing the differentiation favoring exhaustion.
533 Indeed, atypical effector states have been amplified by the specific deletion or overexpression of
534 exhaustion lineage-defining transcription factors(*17, 19*). These and other data(*36*) suggest that
535 the T_{EX} subsets are not entirely devoid of plasticity. It is likely that T cells in various stages of T_{EX}
536 differentiation within tumors may encounter distinct microenvironmental signals that push them
537 towards an enhanced or diminished functional state. While the overarching trajectory of CD8 T
538 cell differentiation in tumors may be set by exhaustion-lineage defining factors, there appear to
539 be local and indeed global peaks and valleys of function that may be determined by additional
540 axes of potency.

541 As exploration of spatial niches of functional immunity continue to drive the field, we posit that this
542 approach to directly mark the potent effectors in the TME may be an important anchoring tool.
543 Detecting, studying and ultimately enhancing functional anti-tumor CD8 T cells will lead to the
544 discovery of novel strategies to drive better patient outcomes.

References:

1. M. L. Broz *et al.*, Dissecting the Tumor Myeloid Compartment Reveals Rare Activating Antigen-Presenting Cells Critical for T Cell Immunity. *Cancer Cell* **26**, 938 (2014).
2. H. Salmon *et al.*, Expansion and Activation of CD103(+) Dendritic Cell Progenitors at the Tumor Site Enhances Tumor Responses to Therapeutic PD-L1 and BRAF Inhibition. *Immunity* **44**, 924-938 (2016).
3. M. J. Pittet, M. Di Pilato, C. Garris, T. R. Mempel, Dendritic cells as shepherds of T cell immunity in cancer. *Immunity* **56**, 2218-2230 (2023).
4. B. Ruffell *et al.*, Macrophage IL-10 blocks CD8+ T cell-dependent responses to chemotherapy by suppressing IL-12 expression in intratumoral dendritic cells. *Cancer Cell* **26**, 623-637 (2014).
5. D. Masopust, S. J. Ha, V. Vezys, R. Ahmed, Stimulation history dictates memory CD8 T cell phenotype: implications for prime-boost vaccination. *J Immunol* **177**, 831-839 (2006).
6. B. B. Au-Yeung *et al.*, A sharp T-cell antigen receptor signaling threshold for T-cell proliferation. *Proc Natl Acad Sci U S A* **111**, E3679-3688 (2014).
7. J. N. Mandl, J. P. Monteiro, N. Vrisekoop, R. N. Germain, T cell-positive selection uses self-ligand binding strength to optimize repertoire recognition of foreign antigens. *Immunity* **38**, 263-274 (2013).
8. A. Schietinger *et al.*, Tumor-Specific T Cell Dysfunction Is a Dynamic Antigen-Driven Differentiation Program Initiated Early during Tumorigenesis. *Immunity* **45**, 389-401 (2016).
9. A. C. Scott *et al.*, TOX is a critical regulator of tumour-specific T cell differentiation. *Nature* **571**, 270-274 (2019).
10. O. Khan *et al.*, TOX transcriptionally and epigenetically programs CD8 + T cell exhaustion. *Nature* **571**, 211-218 (2019).
11. J. C. Beltra *et al.*, Developmental Relationships of Four Exhausted CD8+ T Cell Subsets Reveals Underlying Transcriptional and Epigenetic Landscape Control Mechanisms. *Immunity* **52**, 825-841.e828 (2020).
12. B. Daniel *et al.*, Divergent clonal differentiation trajectories of T cell exhaustion. (2021).
13. W. H. Hudson *et al.*, Proliferating Transitory T Cells with an Effector-like Transcriptional Signature Emerge from PD-1. *Immunity* **51**, 1043-1058.e1044 (2019).
14. E. J. Wherry *et al.*, Molecular signature of CD8+ T cell exhaustion during chronic viral infection. *Immunity* **27**, 670-684 (2007).
15. M. Philip *et al.*, Chromatin states define tumour-specific T cell dysfunction and reprogramming. *Nature* **545**, 452-456 (2017).
16. D. T. Utzschneider *et al.*, Early precursor T cells establish and propagate T cell exhaustion in chronic infection. *Nat Immunol* **21**, 1256-1266 (2020).
17. C. Tsui *et al.*, MYB orchestrates T cell exhaustion and response to checkpoint inhibition. *Nature* **609**, 354-360 (2022).
18. N. Prokhnevska *et al.*, CD8 + T cell activation in cancer comprises an initial activation phase in lymph nodes followed by effector differentiation within the tumor. *Immunity* **56**, 107-124.e105 (2023).
19. Z. Chen *et al.*, TCF-1-Centered Transcriptional Network Drives an Effector versus Exhausted CD8 T Cell-Fate Decision. *Immunity* **51**, 840-855.e845 (2019).
20. A. C. Scott *et al.*, TOX is a critical regulator of tumour-specific T cell differentiation. *Nature* **571**, 270-274 (2019).
21. H. Li *et al.*, Dysfunctional CD8 T Cells Form a Proliferative, Dynamically Regulated Compartment within Human Melanoma. *Cell* **176**, 775-789 e718 (2019).

22. H. E. Ghoneim *et al.*, De Novo Epigenetic Programs Inhibit PD-1 Blockade-Mediated T Cell Rejuvenation. *Cell* **170**, 142-157.e119 (2017).
23. K. Kersten *et al.*, Spatiotemporal co-dependency between macrophages and exhausted CD8+ T cells in cancer. *Cancer Cell* **40**, 624-638.e629 (2022).
24. B. L. Horton *et al.*, Lack of CD8 + T cell effector differentiation during priming mediates checkpoint blockade resistance in non-small cell lung cancer. *Sci Immunol* **6**, eabi8800 (2021).
25. A. C. Y. Chen *et al.*, The aged tumor microenvironment limits T cell control of cancer. *Nat Immunol* **25**, 1033-1045 (2024).
26. K. G. Anderson, I. M. Stromnes, P. D. Greenberg, Obstacles Posed by the Tumor Microenvironment to T cell Activity: A Case for Synergistic Therapies. *Cancer Cell* **31**, 311-325 (2017).
27. J. M. Schenkel *et al.*, T cell memory. Resident memory CD8 T cells trigger protective innate and adaptive immune responses. *Science* **346**, 98-101 (2014).
28. L. K. Mackay *et al.*, Hobit and Blimp1 instruct a universal transcriptional program of tissue residency in lymphocytes. (2016).
29. F. A. Buquicchio *et al.*, Distinct epigenomic landscapes underlie tissue-specific memory T cell differentiation. *Immunity*, (2024).
30. B. Virassamy *et al.*, Intratumoral CD8 + T cells with a tissue-resident memory phenotype mediate local immunity and immune checkpoint responses in breast cancer. *Cancer Cell* **41**, 585-601.e588 (2023).
31. F. Djenidi *et al.*, CD8+CD103+ tumor-infiltrating lymphocytes are tumor-specific tissue-resident memory T cells and a prognostic factor for survival in lung cancer patients. *J Immunol* **194**, 3475-3486 (2015).
32. M. JJ *et al.*, Heterogenous Populations of Tissue-Resident CD8+ T Cells Are Generated in Response to Infection and Malignancy. *Immunity* **52**, (2020).
33. M. Sade-Feldman *et al.*, Defining T Cell States Associated with Response to Checkpoint Immunotherapy in Melanoma. *Cell* **175**, 998-1013.e1020 (2018).
34. S. J. Im *et al.*, Defining CD8+ T cells that provide the proliferative burst after PD-1 therapy. *Nature* **537**, 417-421 (2016).
35. M. L. Burger *et al.*, Antigen dominance hierarchies shape TCF1(+) progenitor CD8 T cell phenotypes in tumors. *Cell* **184**, 4996-5014 e4926 (2021).
36. S. E. McClory *et al.*, The pseudokinase Trib1 regulates the transition of exhausted T cells to a KLR. *Cell Rep* **42**, 112905 (2023).
37. J. C. Beltra *et al.*, Stat5 opposes the transcription factor Tox and rewires exhausted CD8(+) T cells toward durable effector-like states during chronic antigen exposure. *Immunity* **56**, 2699-2718 e2611 (2023).
38. R. C. Lynn *et al.*, c-Jun overexpression in CAR T cells induces exhaustion resistance. *Nature* **576**, 293-300 (2019).
39. H. Seo *et al.*, BATF and IRF4 cooperate to counter exhaustion in tumour-infiltrating CAR T cells. (2021).
40. J. F. Brooks *et al.*, Negative feedback by NUR77/Nr4a1 restrains B cell clonal dominance during early T-dependent immune responses. *Cell Rep* **36**, 109645 (2021).
41. C. Tan *et al.*, NR4A nuclear receptors restrain B cell responses to antigen when second signals are absent or limiting. *Nat Immunol* **21**, 1267-1279 (2020).
42. F. Salerno, M. Turner, M. C. Wolkers, Dynamic Post-Transcriptional Events Governing CD8(+) T Cell Homeostasis and Effector Function. *Trends Immunol* **41**, 240-254 (2020).
43. A. G. Santis, M. López-Cabrera, F. Sánchez-Madrid, N. Proudfoot, Expression of the early lymphocyte activation antigen CD69, a C-type lectin, is regulated by mRNA degradation associated with AU-rich sequence motifs. *Eur J Immunol* **25**, 2142-2146 (1995).

643 44. F. Salerno *et al.*, An integrated proteome and transcriptome of B cell maturation defines
644 poised activation states of transitional and mature B cells. *Nat Commun* **14**, 5116 (2023).
645 45. H. Weerakoon *et al.*, Integrative temporal multi-omics reveals uncoupling of transcriptome
646 and proteome during human T cell activation. *NPJ Syst Biol Appl* **10**, 21 (2024).
647 46. W. DA *et al.*, The Functional Requirement for CD69 in Establishment of Resident Memory
648 CD8+ T Cells Varies with Tissue Location. *Journal of immunology* **203**, (2019).
649 47. C. Castellanos Mdel, S. Lopez-Giral, M. Lopez-Cabrera, M. O. de Landazuri, Multiple cis-
650 acting elements regulate the expression of the early T cell activation antigen CD69. *Eur J*
651 *Immunol* **32**, 3108-3117 (2002).
652 48. J. F. Ashouri, A. Weiss, Endogenous Nur77 Is a Specific Indicator of Antigen Receptor
653 Signaling in Human T and B Cells. *J Immunol* **198**, 657-668 (2017).
654 49. F. Salerno *et al.*, Translational repression of pre-formed cytokine-encoding mRNA
655 prevents chronic activation of memory T cells. *Nat Immunol* **19**, 828-837 (2018).
656 50. A. J. Litterman *et al.*, A global map of RNA binding protein occupancy guides functional
657 dissection of post-transcriptional regulation of the T cell transcriptome. (2018).
658 51. M. J. Moore *et al.*, ZFP36 RNA-binding proteins restrain T cell activation and anti-viral
659 immunity. *Elife* **7**, (2018).
660 52. T. M. McCaughtry, M. S. Wilken, K. A. Hogquist, Thymic emigration revisited. *J Exp Med*
661 **204**, 2513-2520 (2007).
662 53. M. Yukawa *et al.*, AP-1 activity induced by co-stimulation is required for chromatin opening
663 during T cell activation. *J Exp Med* **217**, (2020).
664 54. J. J. Engelhardt *et al.*, Marginating dendritic cells of the tumor microenvironment cross-
665 present tumor antigens and stably engage tumor-specific T cells. *Cancer Cell* **21**, 402-417
666 (2012).
667 55. N. E. Scharping *et al.*, Mitochondrial stress induced by continuous stimulation under
668 hypoxia rapidly drives T cell exhaustion. *Nature Immunology* **22**, 205-215 (2021).
669 56. J. G. Cyster, S. R. Schwab, Sphingosine-1-phosphate and lymphocyte egress from
670 lymphoid organs. *Annu Rev Immunol* **30**, 69-94 (2012).
671 57. R. You *et al.*, Active surveillance characterizes human intratumoral T cell exhaustion. *J*
672 *Clin Invest* **131**, (2021).
673 58. M. Y. Kasmani *et al.*, Clonal lineage tracing reveals mechanisms skewing CD8+ T cell fate
674 decisions in chronic infection. *J Exp Med* **220**, (2023).
675 59. B. C. Miller *et al.*, Subsets of exhausted CD8 + T cells differentially mediate tumor control
676 and respond to checkpoint blockade. *Nat Immunol* **20**, 326-336 (2019).
677 60. J. J. Milner *et al.*, Runx3 programs CD8 + T cell residency in non-lymphoid tissues and
678 tumours. *Nature* **552**, 253-257 (2017).
679 61. B. Boldajipour, A. Nelson, M. F. Krummel, Tumor-infiltrating lymphocytes are dynamically
680 desensitized to antigen but are maintained by homeostatic cytokine. *JCI insight* **1**, e89289
681 (2016).
682 62. L. Zheng *et al.*, Pan-cancer single-cell landscape of tumor-infiltrating T cells. *Science* **374**,
683 abe6474 (2021).
684 63. A. J. Combes *et al.*, Discovering dominant tumor immune archetypes in a pan-cancer
685 census. *Cell* **185**, 184-203.e119 (2022).
686 64. C. U. Blank *et al.*, Defining 'T cell exhaustion'. *Nat Rev Immunol* **19**, 665-674 (2019).
687 65. J. CS *et al.*, An intra-tumoral niche maintains and differentiates stem-like CD8 T cells.
688 *Nature* **576**, (2019).
689 66. T. N. Schumacher, D. S. Thommen, Tertiary lymphoid structures in cancer. *Science* **375**,
690 eabf9419 (2022).
691 67. K. C. Barry *et al.*, A natural killer-dendritic cell axis defines checkpoint therapy-responsive
692 tumor microenvironments. *Nat Med* **24**, 1178-1191 (2018).

68. M. K. Ruhland *et al.*, Visualizing Synaptic Transfer of Tumor Antigens among Dendritic Cells. *Cancer Cell* **37**, 786-799.e785 (2020).
69. Y. S. Tan, Y. L. Lei, Isolation of Tumor-Infiltrating Lymphocytes by Ficoll-Paque Density Gradient Centrifugation. *Methods Mol Biol* **1960**, 93-99 (2019).
70. C. S. McGinnis *et al.*, MULTI-seq: sample multiplexing for single-cell RNA sequencing using lipid-tagged indices. *Nat Methods* **16**, 619-626 (2019).
71. E. Kim *et al.*, Inositol polyphosphate multikinase is a coactivator for serum response factor-dependent induction of immediate early genes. *Proc Natl Acad Sci U S A* **110**, 19938-19943 (2013).
72. A. S. Stephens, S. R. Stephens, N. A. Morrison, Internal control genes for quantitative RT-PCR expression analysis in mouse osteoblasts, osteoclasts and macrophages. *BMC Res Notes* **4**, 410 (2011).
73. A. Dobin *et al.*, STAR: ultrafast universal RNA-seq aligner. *Bioinformatics* **29**, 15-21 (2013).
74. B. Li, C. N. Dewey, RSEM: accurate transcript quantification from RNA-Seq data with or without a reference genome. *BMC Bioinformatics* **12**, 323 (2011).
75. H. G. Othmer, S. R. Dunbar, W. Alt, Models of dispersal in biological systems. *J Math Biol* **26**, 263-298 (1988).
76. R. B. Dickinson, R. T. Tranquillo, Optimal estimation of cell movement indices from the statistical analysis of cell tracking data. AIChE Journal Volume 39, Issue 12. *AIChE Journal*. 1993.

Acknowledgments:

Funding:

National Institutes of Health Grants: NIH R01CA197363 and NIH R37AI052116

AR was supported by a Cancer Research Institute Postdoctoral Fellowship (CRI2940)

KHH was supported by an American Cancer Society and Jean Perkins Foundation Postdoctoral Fellowship

GH was supported by the National Science Foundation Graduate Research Fellowship Program (NSF2034836)

IZL was supported by Emerson Collective Health Research Scholars Program

We thank Dr. Emily Flynn, UCSF for guidance with the CITE-Seq analysis. We thank Dr. Jeroen Roose, UCSF, Dr. Julie Zikherman, UCSF and Dr. Susan Schwab, NYU for discussions and guidance. We thank Dr. Kelly Kersten, Sanford-Burnham Prebys, Dr. Mike Kuhns, University of Arizona and Dr. Miguel Reina-Campos, University of California San Diego, for critical reading of the manuscript. We also thank Dr. Reina-Campos for sharing data from Zheng et.al in an analysis-ready format. We thank members of the Krummel lab for their inputs to the manuscript.

730

731 ***Author Contributions:***

732 Conceptualization: AR, MFK

733 Experimentation: AR, MB, GH, LFP, IZL

734 Mouse scSeq: KHH, AR

735 Human tumor data analysis: AR, AJC, BS

736 Human tumor data collection: VD, BD, AJC

737 Funding acquisition: MFK, AR, KHH

738 Writing: AR, MFK

739 Supervision: MFK

740

741 ***Competing Interests:***

742 The authors declare no competing interests

743 ***Data materials availability:***

744 Relevant data will be made publicly available before publication in its final form. Meanwhile, data
745 will be available upon reasonable request, please contact the authors directly.

746 **List of Supplementary Materials:**

747 Materials and Methods

748 Fig. S1-S10

Figures and Figure Legends:

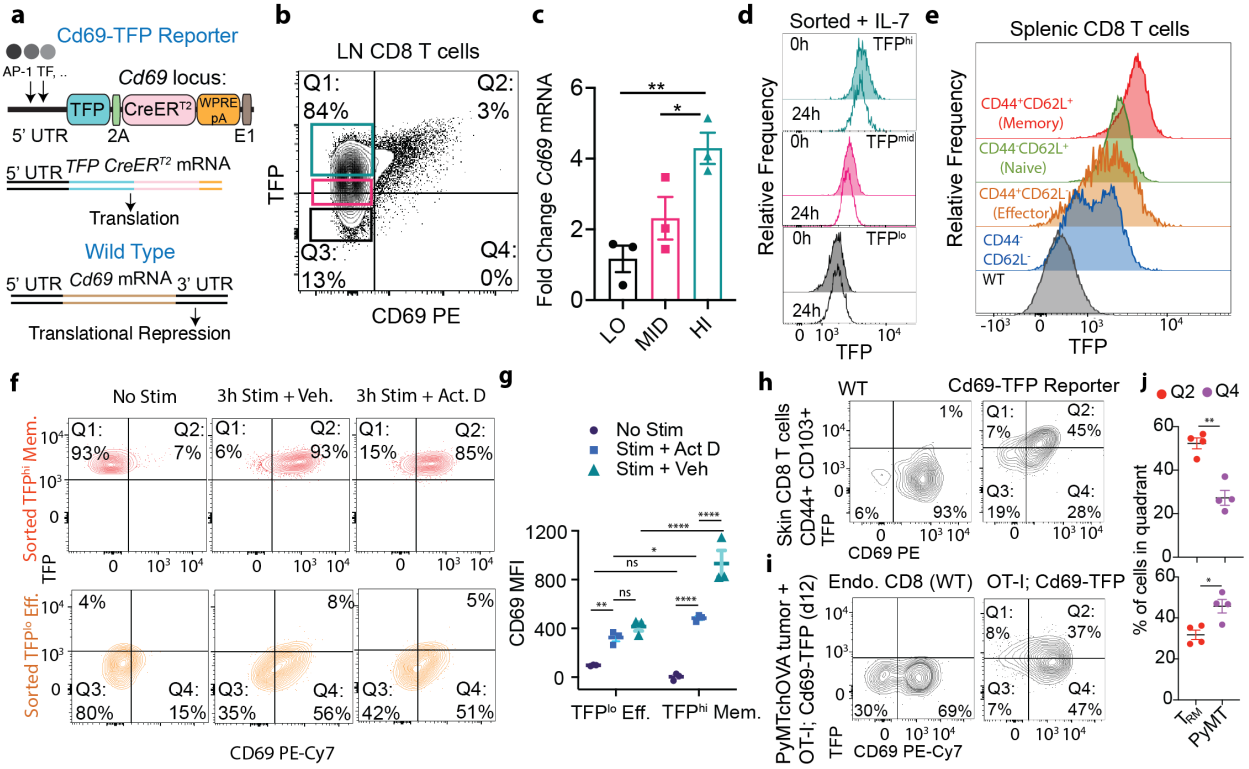

Fig.1: Distinct expression of Cd69 transcriptional reporter and CD69 protein in CD8 T cells **(a)** Design of the TFP-2A-CreER^{T2}-WPRE-pA reporter knocked into the 5' UTR of the *Cd69* locus for transcriptional reporting; **(b)** TFP and surface CD69 expression in homeostatic lymph node (LN) CD8 T cells; color-coded boxes indicate sorted TFP 'LO', 'MID' and 'HI' cell populations, assayed for **(c)** Cd69 mRNA expression by qPCR; **(d)** histograms of TFP expression from sorted TFP^{hi} (top 20%), TFP^{mid} (middle 30%) and TFP^{lo} (bottom 20%) of splenic and lymph node-derived CD8 T cells at 0h and 24h post sort, resting in IL-7; **(e)** representative histograms of TFP expression in splenic CD8 T cells of different phenotypes (as indicated in the figure panel) from an unchallenged Cd69-TFP reporter mouse; **(f)** flow cytometry plots of TFP and CD69 in sorted TFP^{lo} Effector (CD44+CD62L-) and TFP^{hi} Memory (CD44+CD62L+) homeostatic CD8 T cells without stimulation (No Stim), 3h αCD3+αCD28 stimulation + DMSO (3h Stim + Vehicle) or 5μg/mL Actinomycin D (3h Stim + Act.D) and **(g)** CD69 MFI of the same across conditions; TFP and CD69 expression on **(h)** skin-resident CD44+CD103+ CD8 T cells in 6 month old unchallenged WT control and Cd69-TFP reporter mice; **(i)** Endogenous and adoptively transferred OT-I; Cd69-TFP reporter CD8 T cells in PyMTchOVA(*54*) tumors 12d post adoptive transfer and **(j)** corresponding quantification of the percentage of cells in Q2 (TFP^{hi}CD69+) and Q4 (TFP^{lo}CD69+) states in the same; Plots show mean +/- SEM; TFP negative gates derived from corresponding WT controls; null hypothesis testing by unpaired t test, adjusted for multiple comparisons, n=3 biological replicates representative of at least 2 independent experiments. *p<0.05, **p<0.01, ***p<0.001, ****p<0.0001, ns = no significance.

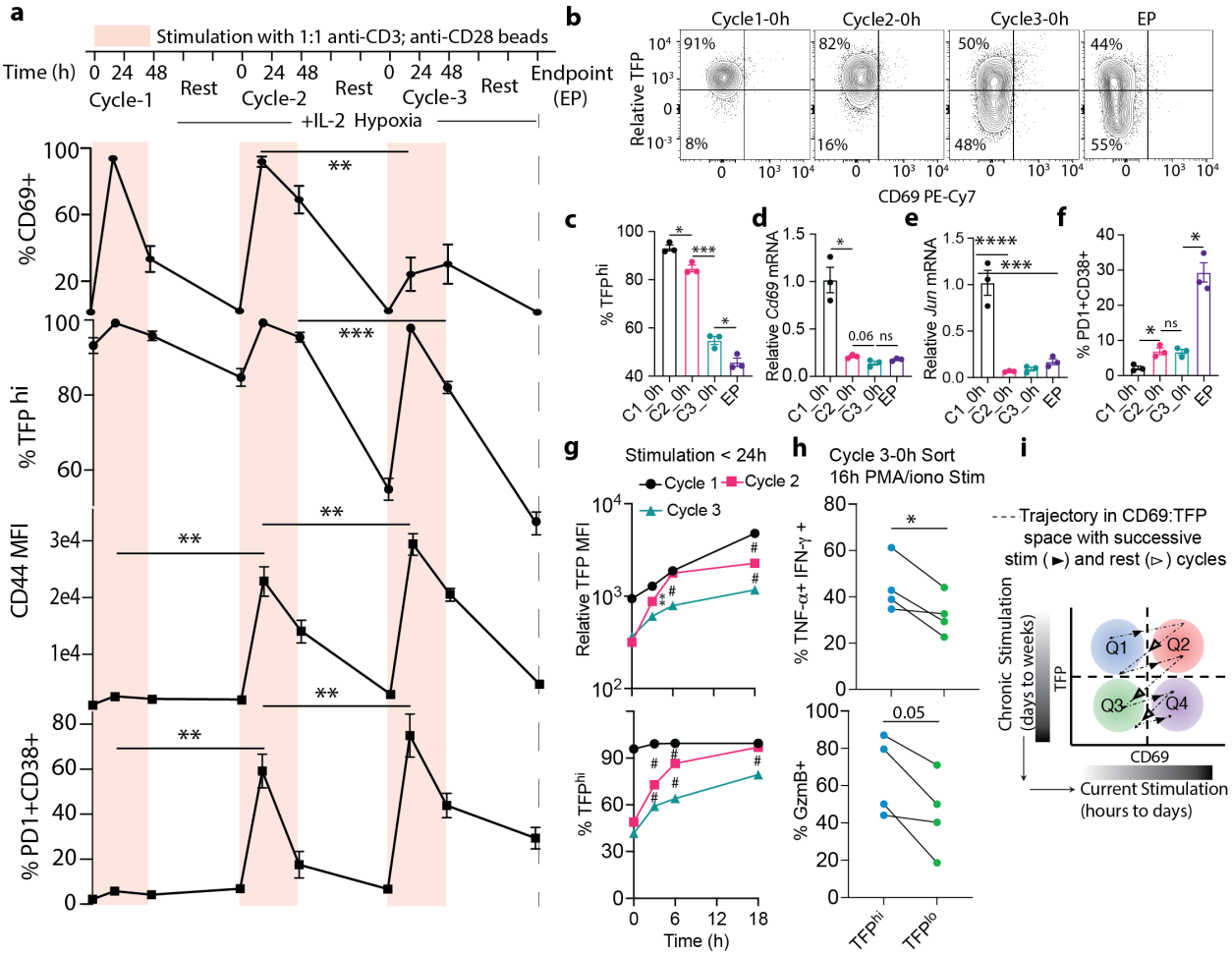

Fig.2: Repeated TCR stimulation drives down Cd69 transcription and the reporter TFP in CD8 T cells: (a) %CD69+, %TFP^{hi}, CD44 MFI, %PD1^{+}CD38^{+} of freshly isolated CD8 T cells through successive cycles of 48h stimulation and 72h resting in hypoxia + IL-2; **(b)** representative flow cytometry plots showing relative TFP (TFP normalized to WT control) and CD69 expression at the beginning of cycles 1, 2, 3 and endpoint (EP); **(c)** %TFP^{hi}, **(d)** *Cd69* mRNA and **(e)** *Jun* mRNA by qPCR, **(f)** %PD1^{+}CD38^{+} at the same time points; **(g)** TFP expression by MFI and %TFP^{hi} with 0, 3, 6 and 18h stimulation at Cycle1, 2 and 3h; **(h)** Cytokine and GzmB expression in sorted TFP^{hi} and TFP^{lo} cells from the 'Cycle 3-0h' condition, restimulated 16h with PMA/ionomycin; **(i)** schematic showing the trajectory of CD8 T cells within the TFP:CD69 states (quadrants) with successive stimulation and rest, providing a reading of history of stimulation. *p<0.05, **p<0.01, ***p<0.001, ****p<0.0001, ns = no significance, #p<0.001 in (g).

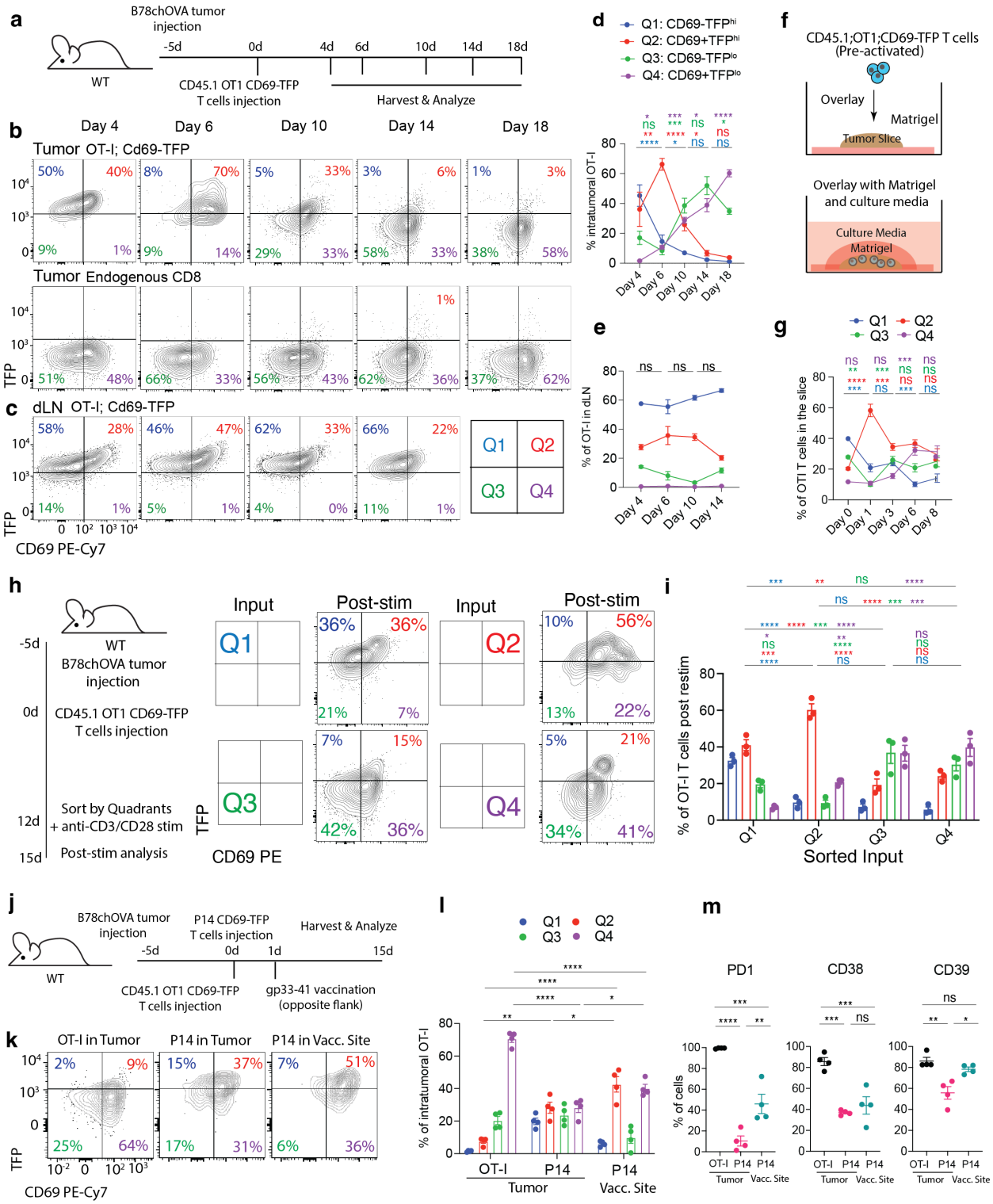

Fig. 3: Chronic antigen exposure in tumor leads to decline in TFP expression in CD8 T cells **(a)** Experimental schematic to track antigen-specific T cells in B78chOVA tumors over time; Flow cytometry plots showing TFP and CD69 expression of **(b)** adoptively transferred OT-I T cells and endogenous CD8 T cells from B78chOVA tumors and **(c)** OT-I T cells in corresponding tumor-draining lymph nodes (dLN) over time; corresponding CD69:TFP quadrant (Q1-Q4) distribution

for the same OT-I T cells in the **(d)** tumor and **(e)** tdLN; **(f)** Schematic representation of long-term tumor slice culture setup; pre-activated: 48h stimulation with αCD3+αCD28 followed by 48h rest in IL-2; **(g)** CD69:TFP quadrant distribution of slice-infiltrating OT-I T cells over time; **(h)** representative flow cytometry plots and **(i)** quantification of resultant quadrant distribution of OT-I T cells sorted by their Cd69:TFP quadrants from B78chOVA tumors (Q2-Q4) or dLN (Q1) 12d post adoptive transfer, and restimulated with anti-CD3/anti-CD28 for 3d; **(j)** Experimental schematic of tumor injection and contralateral vaccination with distinct antigen specificities (OT-I and P14; P14 cells are 20-25% less TFP+ than OT-Is at baseline before injection); **(k)** Flow cytometry plots showing TFP and CD69 profiles of OT-I, P14 T cells in the OVA+ tumor and P14 T cells at the gp33-41 vaccination (vacc.) site; **(l)** CD69:TFP quadrant distribution of the same and **(m)** PD1, CD38 and CD39 expression among the same three groups.
Representative data from 2-3 independent experiments, 3-4 mice or 5-6 slices/timepoint/experiment, pre-slice-overlay samples in duplicate, plots show mean +/- SEM. ****$p<0.0001$, ***$p<0.001$, **$p<0.01$, *$p<0.05$ in one-way ANOVA for each quadrant with pairwise multiple comparisons as shown using the post-hoc Tukey test in j, k, and 2-way ANOVA with post-hoc Tukey test between pair-wise timepoints (d-g) and 2-way ANOVA with false discovery rate correction for comparisons among inputs (i).

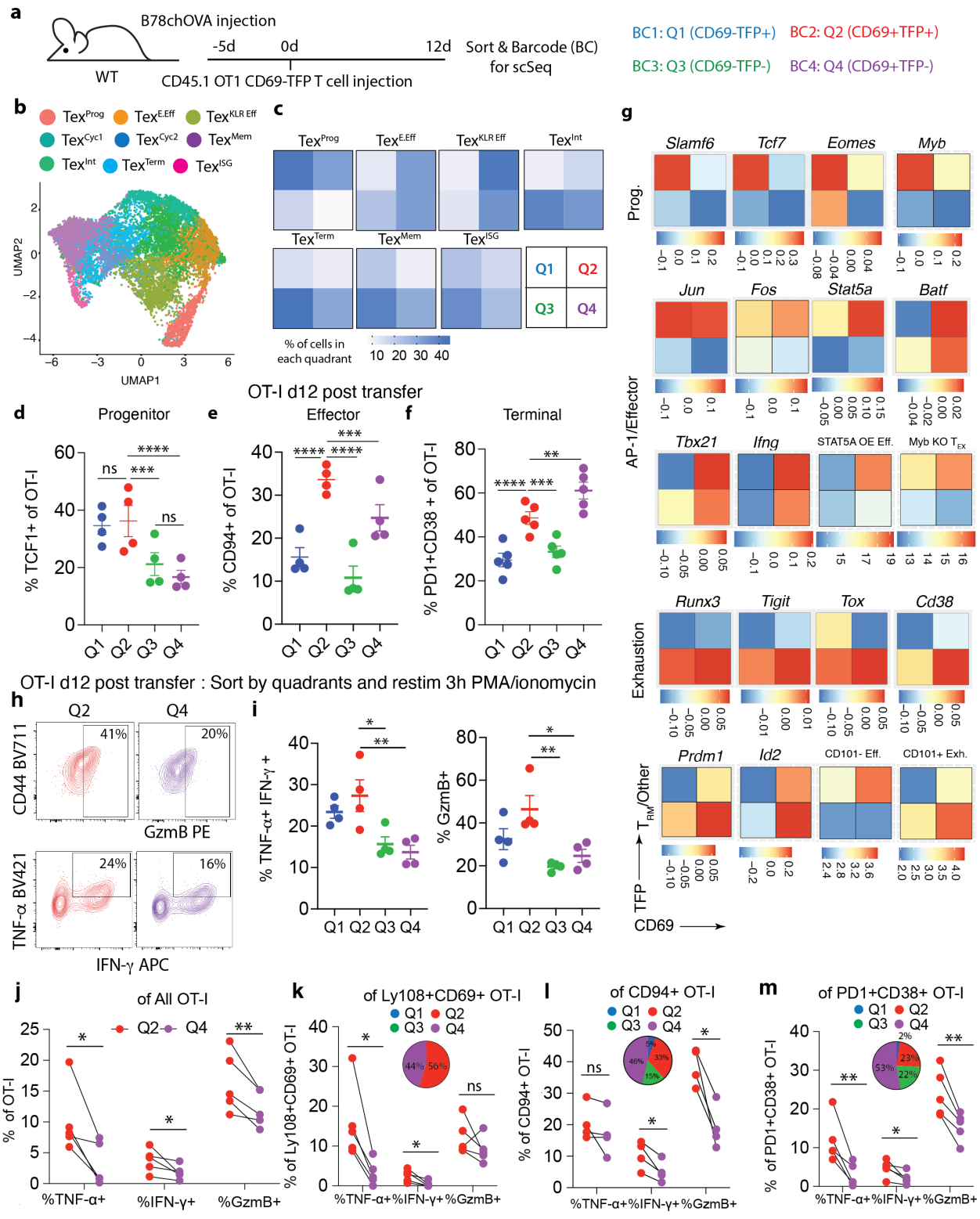

Fig. 4: TFP^hi^CD69+ (Q2) marks a potent functional state of antigen-specific CD8 T cells within tumors: (a) Experimental schematic for single cell transcriptomic profiling of intratumoral OT-I T cells sorted by CD69:TFP quadrants; **(b)** UMAP representation of the scSeq data color-coded by computationally-derived clusters; **(c)** Heatmap showing percentage of cells that belong

to the four CD69:TFP quadrants Q1-Q4 within each cluster; distribution of **(d)** percentage of cells bearing progenitor (TCF1+), **(e)** effector (KLRD1, or CD94+) and **(f)** terminal exhaustion (PD1+CD38+) markers within each CD69:TFP quadrant; **(g)** Heatmaps showing distribution of transcripts (canonical progenitor, AP-1/Effector, Exhaustion and tissue-resident memory related genes) and transcriptomic signatures (corresponding to Stat5a overexpressing effectors(*37*), Myb KO(*17*), CD101-Tim3+ and CD101+Tim3+(*13*) exhausted CD8 T cells) in the four CD69:TFP quadrants; **(h)** flow cytometry plots showing representative GzmB and cytokine expression in Q2 vs. Q4 intratumoral OT-Is from B78chOVA tumors 12d post adoptive transfer which were sorted and then restimulated for 3h in PMA/ionomycin and **(i)** corresponding bar graph quantification of the same; **(j)** cytokine and GzmB expression in intratumoral OT-I T cells at baseline (d12 post adoptive transfer) in the Q2 vs. Q4 activation state; cytokine and GzmB expression of Q2 vs. Q4 OT-I T cells within **(k)** Ly108+CD69+(*11*), **(l)** CD94+ and **(m)** PD1+CD38+ intratumoral OT-I subsets with inset pie chart showing the percentage of cells in each quadrant) within the corresponding subsets. Bar plots show mean +/- SEM; null hypothesis testing by ratio paired t test (i-m), RM ANOVA followed by post-hoc paired t-tests corrected for multiple comparisons (d-f). *$p<0.05$, **$p<0.01$, ns = no significance.

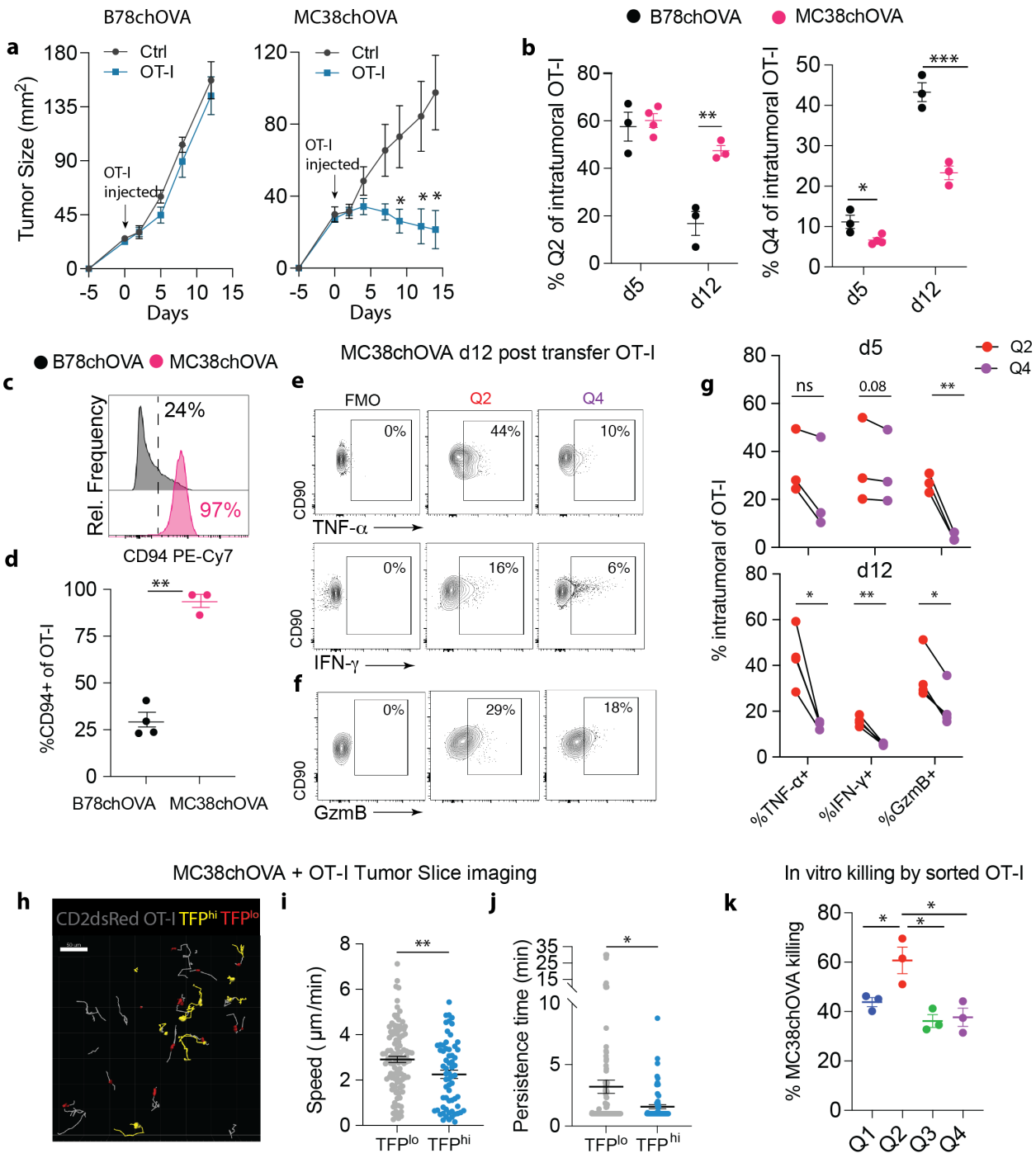

Fig. 5: Evidence of TFP^{hi}CD69+ (Q2) CD8 T cell function in a model of tumor regression: **(a)** Tumor growth curves of B78chOVA and MC38chOVA with and without OT-I transfer 5 days post tumor injection, as indicated by arrows (n=5-6/group); **(b)** quantification of the percentage of Q2 and Q4 cells at d5 and d12 post adoptive transfer in the two tumor models; **(c)** typical CD94 expression in Intratumoral OT-Is in B78chOVA and MC38chOVA tumors d12 post-adoptive transfer and **(d)** corresponding quantification; **(e-g)** Flow cytometry plots showing **(e)** intracellular cytokine and **(f)** GzmB expression in OT-I T cells in the Q2 vs. Q4 state d12 post adoptive transfer in MC38chOVA tumors and **(g)** quantification of the same at d5 and d12; **(h)** representative tumor

slice image showing cell migration tracks associated with TFP^{lo} (red) and TFP^{hi} (yellow) CD2dsRed;OT-I T cells and corresponding quantification of **(i)** cell speed and **(j)** persistence of migration; **(k)** in vitro killing of MC38chOVA cells by OT-I T cells sorted by CD69:TFP quadrants from MC38chOVA tumors 8d after adoptive transfer; Bar plots show mean +/- SEM; null hypothesis testing by ratio paired t test (g), ANOVA with post-hoc Holm-Šídák test (b, k), unpaired t test (c) and Mann-Whitney test (i, j). *p<0.05, **p<0.01.

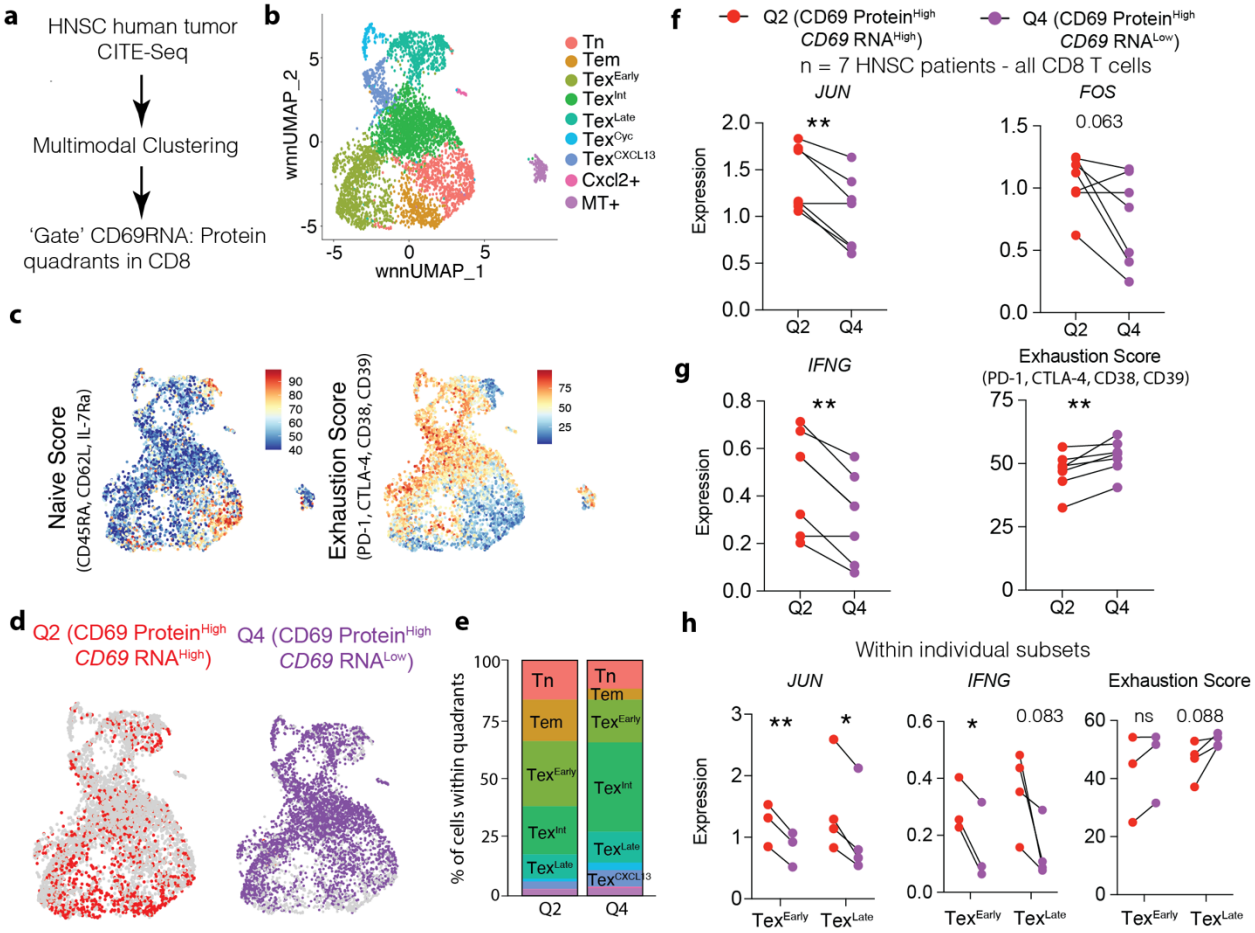

Fig. 6: Simultaneous marking of Cd69 RNA and protein expression by CITE-Seq delineates intratumoral CD8 T cell activation states in head and neck squamous cell carcinoma: (a) Schematic description of human HNSC tumor CITE-Seq analysis; **(b)** UMAP showing weighted nearest neighbor (WNN) determined clusters by multimodal RNA and Protein analysis; **(c)** overlay of Naïve and Exhaustion score and **(d)** that of Q2 and Q4 cells (determined by gating on CD69 Protein and RNA) on the WNN-UMAP; **(e)** Stacked barplot showing relative contribution of the various subsets to the Q2 and Q4 states, as defined by Cd69 RNA and CD69 surface protein; Patient-by-patient expression of **(f)** *JUN* and *FOS,* **(g)** *IFNG* and Exhaustion markers in Q2 and Q4 CD8 T cells and **(h)** *JUN, IFNG,* Exhaustion markers between Q2 and Q4 within individual Tex^{Early} and Tex^{Late} subsets. *p<0.05, **p<0.01, ns = no significance by paired t tests (f-h).

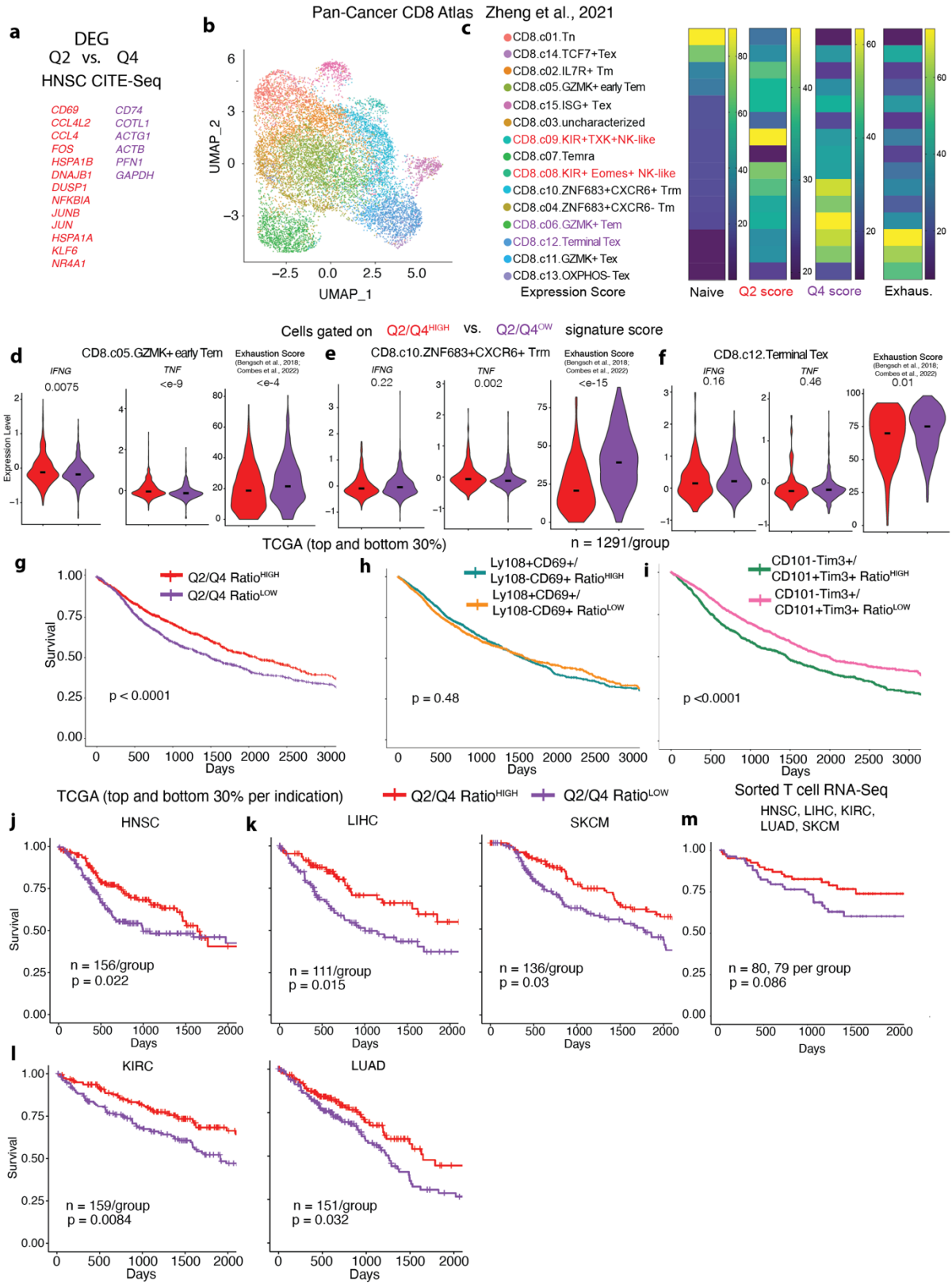

Fig. 7: Transcriptomic signatures of Cd69RNA^{hi}CD69Protein^{hi} (Q2) state associates with anti-tumor effector function in human cancers: (a) Differentially expressed genes of cells in

Q2 vs. Q4 (|avg_logFC|>0.4, pval_adj <0.01) from the HNSC CITE-Seq data in Fig. 6 used to generate Q2 and Q4 signature scores; **(b)** UMAP representation of computationally-derived subsets among CD8 T cells in a pan-cancer T cell atlas(*62*), color-coded subset labels are as shown in (c); **(c)** Heatmap showing Naïve (*Sell, Il7r, Tcf7, Lef1, Ccr7*), Q2 (from a), Q4 (from a) and exhaustion(*63*) signature scores in the major CD8 T cell subsets from the same pan-cancer dataset, top two subsets in Q2 and Q4 score expression are labeled red and purple respectively, clusters are arranged in descending order of expression of the naïve score; expression of *IFNG*, *TNF* and Exhaustion signature score within the **(d)** Early Tem, **(e)** CXCR6+ Trm and **(f)** Terminal Tex clusters grouped by Q2/Q4^{high} and Q2/Q4^{low} (top and bottom 33% of the Q2 score/Q4 score ratio); **(g-i)** Kaplan-Meier survival curves from a quality controlled subset of TCGA data (*63*) corresponding to all indications stratified by the ratio of **(g)** Q2 and Q4 expression scores, **(h)** signatures corresponding to Ly108+CD69+ and Ly108-CD69+ subsets (Signature 1 and Signature 7 from (*11*)) and **(i)** CD101-Tim3+ effector and CD101+Tim3+ terminal subsets (*13*); Kaplan-Meier survival curves from a curated list of TCGA data(*63*) corresponding to **(j)** HNSC, **(k)** LIHC, SKM **(l)** KIRC and LUAD indications, patients stratified by the ratio of Q2 and Q4 expression scores; **(m)** Kaplan-Meier survival curves from a cohort of patients of combined HNSC, LIHC, SKM, KIRC and LUAD indications, with patients stratified by the ratio of Q2 and Q4 expression scores from bulk RNA-Seq of sorted T cells(*63*) number of patients per group and p-value for log-rank tests are noted in g-l and p-values for Wilcoxon test in d-f are noted. Black bars represent median in d-f.

Graphical Abstract

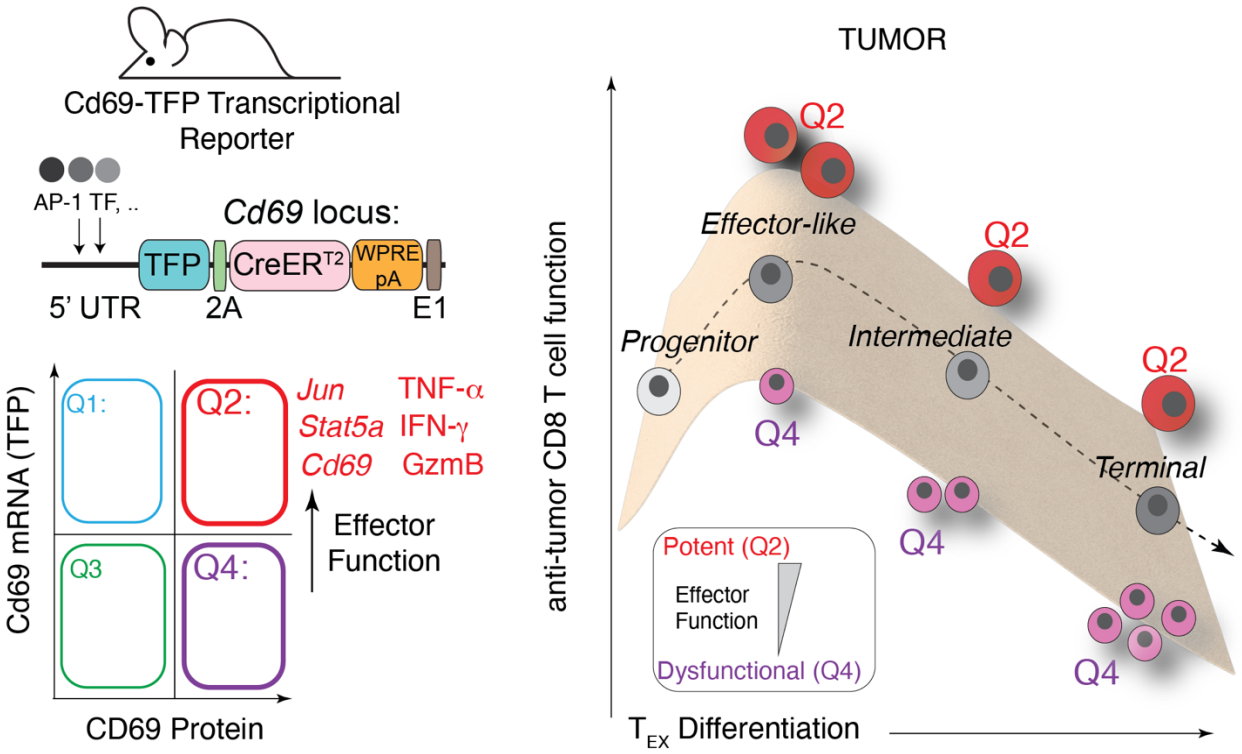

Supplementary Materials for

Multimodal delineation of a layer of effector function among exhausted CD8 T cells in tumors

Arja Ray[1,2], Molly Bassette[1,2], Kenneth H. Hu[1,2,#], Lomax F. Pass[1,2], Bushra Samad[2,3], Alexis Combes[1,2,3,5], Vrinda Johri[2,3], Brittany Davidson[2,3], Katherine Wai[6], Patrick Ha[6], Grace Hernandez[4], Itzia Zaleta-Linares[1,2], Matthew F. Krummel[1,2*]

Affiliations:

[1]Department of Pathology, [2]ImmunoX Initiative, [3]UCSF CoLabs, [4]Department of Anatomy, [5]Department of Medicine, [6]Department of Otolaryngology Head and Neck Surgery, University of California, San Francisco, CA 94143, USA. [#]Current Address: Department of Immunology, The University of Texas MD Anderson Cancer Center and James P Allison Institute

***Corresponding Author:**
Matthew F. Krummel, Ph.D.
513 Parnassus Avenue, HSW 512
San Francisco, CA 94143-0511
matthew.krummel@ucsf.edu
Tel: (415) 514-3130
Fax: (415) 514-3165

934 **Materials and Methods**

935 ***Mice:*** All mice were treated in accordance with the regulatory standards of the National Institutes
936 of Health and American Association of Laboratory Animal Care and were approved by the UCSF
937 Institution of Animal Care and Use Committee. Cd69-TFP-CreER^{T2} (denoted as Cd69-TFP) mice
938 in the C57BL6/J background were custom-generated from Biocytogen Inc. and then maintained
939 heterozygous (bred to C57BL6/J wild type mice) at the UCSF Animal Barrier facility under specific
940 pathogen-free conditions. C57BL6/J (wild type; WT), C57BL6/J CD45.1 (B6.SJL-Ptprc^{a}
941 Pepc^{b}/BoyJ), OT-I (C57BL/6-Tg(TcraTcrb)1100Mjb/J) mice were purchased for use from Jackson
942 Laboratories and maintained in the same facility in the C57BL6/J background. For adoptive
943 transfer experiments, CD45.1^{het}; OT-I^{het}; Cd69-TFP^{het} (denoted simply as CD45.1; OT1; Cd69-
944 TFP) mice were used. Mice of either sex ranging in age from 6 to 14 weeks were used for
945 experimentation. For experiments using the transgenic PyMTchOVA strain(*54*), mammary tumor-
946 bearing females in the age range of 15 to 24 weeks were used. Adoptive transfer of T cells in
947 these mice were done when mice developed at least 2 palpable tumors (> 25-30mm^2).

948 **Mouse tumor digestion and flow cytometry:** Tumors from mice were processed to generate
949 single cell suspensions as described previously(*67*). Briefly, tumors were isolated and
950 mechanically minced on ice using razor blades, followed by enzymatic digestion with 200 µg/mL
951 DNAse (Sigma-Aldrich), 100U/mL Collagenase I (Worthington Biochemical) and 500U/mL
952 Collagenase IV (Worthington Biochemical) for 30 min at 37°C while shaking. Digestion was
953 quenched by adding excess 1X PBS, filtered through a 100µm mesh, spun down and red blood
954 cells were removed by incubating with RBC lysis buffer (155 mM NH_4Cl, 12 mM $NaHCO_3$, 0.1 mM
955 EDTA) at room temperature for 10 mins. The lysis was quenched with excess 1X PBS, spun down
956 and resuspended in FACS buffer (2mM EDTA + 1% FCS in 1X PBS) to obtain single cell
957 suspensions. Similarly, tumor draining lymph nodes (dLN) were isolated and mashed over 100µm
958 filters in PBS to generate single cell suspensions.

959 For each sample, 2.5-3 million cells/sample were stained in a total of 50µL of antibody mixture for
960 flow cytometry. Cells were washed with PBS prior to staining with Zombie NIR Fixable live/dead
961 dye (1:500) (Biolegend) for 20 min at 4°C. Cells were washed in FACS buffer followed by surface
962 staining for 30 min at 4°C with directly conjugated antibodies diluted in FACS buffer containing
963 1:100 anti-CD16/32 (Fc block; BioXCell) to block non-specific binding. Antibody dilutions ranged
964 from 1:100-1:400, optimized separately. After surface staining, cells were washed again with
965 FACS buffer. For intracellular staining, cells were fixed for 20 min at 4°C using the IC Fixation
966 Buffer (BD Biosciences) and washed in permeabilization buffer from the FoxP3 Fix/Perm Kit (BD
967 Biosciences). Antibodies against intracellular targets were diluted in permeabilization buffer
968 containing 1:100 Fc Block and cells were incubated for 30 min at 4°C followed by another wash
969 prior to readout on a BD LSRII or Fortessa Cytometer.

970 **Processing and flow cytometry analysis of other mouse organs:** To phenotype T cells under
971 from lymphoid organs homeostasis, spleen and inguinal, mesenteric and brachial lymph nodes
972 were isolated and mashed over 100µm filters washed with 1X PBS to generate single cell
973 suspension of lymphocytes. For splenic suspensions, RBC lysis was performed as described
974 above before staining for flow cytometry.

975 To profile thymocytes, thymus was isolated, cut into small pieces with a razor blade and minced
976 by using gentleMACS dissociator (Miltenyi Biotec) in RPMI. Next, the mixture was spun down and
977 resuspended in the digestion mixture described above and allowed to digest with shaking at 37°C
978 for 20 mins, following which, the remaining tissue was either minced again using the gentleMACS
979 dissociator and/or directly mashed over a 100µm filter in FACS buffer to generate a single cell
980 suspension, ready to be processed for staining and flow cytometry.

981 Skin digestion was done as previously described(*68*). Briefly, mice are shaved and depilated prior
982 to removal of dorsal skin. The skin was then rid of fat, minced with scissors and razor blade in the
983 presence of 1 ml of digest media (2 mg/ml collagenase IV (Roche), 1 mg/ml hyaluronidase

984 (Worthington), 0.1 mg/ml DNase I (Roche) in RPMI-1640 (GIBCO). The minced skin was then
985 moved to a 50 ml conical with 5 ml additional digest solution and incubated at 37°C for 45 min
986 with shaking and intermittent vortexing before being washed and passed through a 70μm strainer
987 prior to staining. TFP high vs. low gates were drawn by using a side-by-side WT control or using
988 endogenous CD8 T cells in the context of adoptive transfer into a tumor-bearing mouse.

989 **Tumor injections and adoptive transfer of CD8 T cells into tumors:** The B78chOVA and
990 MC38chOVA cancer cell lines, as previously described(*23, 67*), were generated by incorporating
991 the same mcherry-OVA construct used to establish the PyMTchOVA spontaneous mouse
992 line(*54*). For tumor injections, the corresponding cells were grown to near confluency (cultured in
993 DMEM with 10% FCS (Benchmark) and 1% PSG (Gibco)) and harvested using 0.05% Trypsin-
994 EDTA (Gibco) and washed 3x with PBS (Gibco). The number of cells to be injected per mouse
995 was resuspended in PBS and mixed in a 1:1 ratio with Growth Factor Reduced Matrigel (Corning)
996 to a final volume of 50μL per injection. The mixture was injected subcutaneously into the flanks
997 of anesthetized and shaved mice. Tumors were allowed to grow for 14–21 days unless otherwise
998 noted, before tumors and tumor-draining lymph nodes were harvested for analysis. CD8 T cells
999 were isolated from CD45.1;OT-1;Cd69-TFP mice using the EasySep Negative Selection Kit (Stem
1000 Cell Bio), resuspended in 1X PBS at 10X concentration 100μL was injected into each tumor-
1001 bearing mice. For B78chOVA and PyMTchOVA tumors, 1 million and for MC38chOVA tumors,
1002 200,000 CD8 T cells were injected retro-orbitally into each mouse either 5d (B78chOVA and
1003 MC38chOVA) post tumor injection or when mice had at least 2 palpable tumors (PyMTchOVA).
1004 Tumor measurements were done by measuring the longest dimension (length) and approximately
1005 perpendicular dimension (width) using digital calipers, rounded to one decimal place each.

1006 **Contralateral tumor injection and vaccination:** 5 days post B78chOVA tumor injection, equal
1007 numbers (1 million) CD8 T cells from a CD45.1;OT-I;Cd69TFP and P14;Cd69TFP mice were
1008 injected retroorbitally into each mice. Next day, gp33-41 subcutaneous peptide (Anaspec)

1009 vaccination was injected contralaterally to the tumor, with 50µg peptide + 50µL Common Freund's
1010 Adjuvant (CFA, Sigma) along with 50µL PBS for a total volume of 100µL. The vaccination site
1011 was identified by a white, hardened subcutaneous mass and isolated and processed similarly to
1012 the tumor for flow cytometry.

1013 **In vitro stimulation of naïve CD8 T cells:** CD8 T cells were isolated from Cd69-TFP or WT mice
1014 as described above and plated in a 96 well round bottom plate (Corning) at 80,000 cells/well in T
1015 cell media-RPMI (Gibco) + 10% FCS (Benchmark) + Penicillin/Streptomycin + Glutamine (Gibco).
1016 TCR stimulation was induced by adding anti-CD3/CD28 Dynabeads (Applied Biosystems) at the
1017 concentration of 2µL per 80,000 cells (1:1 ratio of cells:beads), the plate was briefly spun down
1018 to bring cells and beads together before incubation at 37°C for varying lengths of time. 55µM β-
1019 mercaptoethanol (BME; Gibco) was added to the T cell media during stimulation. For repeated
1020 stimulation assays, 2 wells of each sample at every time point were pooled for mRNA isolation
1021 and qRT-PCR, while 2 other wells were used as duplicates for flow cytometry. After each cycle,
1022 beads taken off each well and replated for resting in T cell media containing 10 U/mL of
1023 Interleukin-2 (IL-2; Peprotech). To restart each stimulation cycle, cells from each biological
1024 replicate were pooled, counted and Dynabeads were added at the appropriate concentration for
1025 a 1:1 ratio and redistributed into wells for incubation. To assay shorter stimulation times (3, 6,
1026 18h), the same repeated stimulation and rest experiment was carried out but analyzing cells by
1027 flow cytometry at these early stimulation time points at each cycle.

1028 For cytokine production assays, cells at the beginning of Cycle 3 were sorted by TFPhi vs. lo
1029 levels, with the non-reporter expressing control cells used to set the gate. Sorted cells were plated
1030 in a 96-well V-bottom plate either in T cell media or T cell media containing PMA (50 ng/mL;
1031 Sigma-Aldrich), Ionomycin (500ng/mL; Invitrogen) + Brefeldin A (3µg/mL; Sigma-Aldrich) and
1032 BME (Gibco) for 3h, before cells were collected for surface and intracellular staining for cytokines
1033 and granzyme B.

1034 **Sorting and qPCR, resting or restimulation of homeostatic CD8 T cells:** To sort sufficient
1035 CD8 T cells from homeostatic lymphoid organs, CD8 T cells were first isolated from spleens and
1036 inguinal, brachial, mesenteric lymph nodes Cd69-TFP or WT mice using the EasySep Negative
1037 selection kit. These cells were then sorted on TFP^{hi} (top 15%), TFP^{mid} (middle 30%) and TFP^{lo}
1038 (bottom 15%) from each mouse separately and rested in T cell media containing 10 U/mL
1039 Interleukin-7 in a 96 well round bottom plate and assayed at 0, 24 and 48h. Likewise, for qPCR
1040 analysis of populations high, mid and low for TFP, these populations were sorted into cold T cell
1041 media, pelleted and subjected to RNA extraction and qPCR with primers for Cd69 and 18s rRNA
1042 as the reference gene. For the sort and restimulation experiment, Memory (CD44+CD62L+) TFP^{hi}
1043 cells and Effector (CD44+CD62L-) TFP^{lo} cells were sorted and incubated in T cell media + 55μM
1044 BME containing 1:1 anti CD3/CD28 Dynabeads in a 96 well round bottom plate with either 5μg/mL
1045 Actinomycin D (Sigma) in DMSO or DMSO alone (vehicle) for 3h, before profiling by flow
1046 cytometry. De novo CD69 surface expression was measured by the difference of CD69 MFI
1047 between the vehicle and Actinomycin D treated groups.

1048 **Restimulation and cytokine production of intratumoral CD8 T cells:** OT-I T cells from
1049 B78chOVA tumors were sorted on a BD FACSAria Fusion or BD FACSAria2 (BD Biosciences) at
1050 d11-d13 post adoptive transfer of CD8 T cells from CD45.1; OT-I; Cd69-TFP mice, as described
1051 above. To prepare CD45-enriched fractions(*69*), tumors were digested as described above into
1052 single cell suspensions, centrifuged and resuspended in 30mL room temperature (RT) RPMI
1053 1640. Then, 10mL Ficoll-Premium 1.084 (Cytiva) was carefully underlaid and the tubes
1054 centrifuged at 1025g for 20 mins at RT without braking. The resulting interface-localized cells
1055 were pipetted out, diluted in equal volume RPMI and centrifuged at 650g for 5 mins to collect the
1056 cells. This constituted a CD45-enriched fraction which was then processed for staining and FACS.
1057 The four CD69:TFP quadrants were sorted from each tumor sample (cells from 2-3 tumor samples
1058 were pooled for a single biological replicate) into serum-coated microcentrifuge tubes containing

1059 cold T cell media. These were subsequently plated in a 96-well V-bottom plate either in T cell
1060 media or T cell media containing PMA (50 ng/mL; Sigma-Aldrich), Ionomycin (500ng/mL;
1061 Invitrogen) + Brefeldin A (3µg/mL; Sigma-Aldrich) and BME (Gibco) for 3h, before cells were
1062 collected for surface and intracellular staining for cytokines and granzyme B.

1063 To determine the conversion trajectory of Cd69:TFP quadrants, intratumoral OT-I T cells were
1064 similarly sorted by Cd69:TFP gating, and restimulated with excess anti CD3/CD28 Dynabeads in
1065 a 96 well V-bottom plate for 3d. Due to dearth of Q1 cells in the tumors at d12, we sorted those
1066 cells from the dLN instead. The resulting re-stimulated cells were assayed by flow cytometry to
1067 determine converted Cd69:TFP quadrant distributions from each group.

1068 **Long-term ex vivo tumor slice overlay:** Tumor slice overlay cultures were adapted, modified
1069 and extended from previous work(*57*). For tumor slice overlay cultures, B78chOVA tumors were
1070 injected bilateral subcutaneously into the flank of anesthetized and shaved mice. Tumors were
1071 allowed to grow for 11 – 13 days. 96 hours prior to tumor harvest and slicing, CD8 T cells were
1072 isolated from CD45.1;OT-1;Cd69-TFP mice, as described above. Isolated CD8 T cells were
1073 activated via 1:1 culture with Dynabeads Mouse T-Activator CD3/CD28 (Invitrogen) in T cell
1074 media + BME in 96 well U-bottom plates for 48 hours. After activation, T cells were removed from
1075 Dynabeads rested in T cell media with supplemented 10 U/mL IL-2 (PeproTech) for 48 hours
1076 before use. For gating TFP high vs. low cells, CD8 T cells from CD45.1; OT-I mice were subjected
1077 to similar pre-treatment and profiled by flow cytometry side-by-side along with the CD45.1;OT-
1078 1;Cd69-TFP CD8 T cells at d0.

1079 For slicing, tumors were harvested and stored in cold RPMI until use. Each well of a 24 well plate
1080 was pre-filled with cold RPMI and stored on ice. Tumors were embedded in 1.5-2% agarose gel,
1081 allowed to solidify, and sliced at a thickness of 350 – 400µm using a Compresstome VF310-0Z
1082 Vibrating Microtome (Precisionary). Slices were immediately stored in pre-filled 24 well plate on
1083 ice until use.

1084 For the slice overlay, each well of a 24 well plate was pre-coated with 30μL of 1 part culture
1085 medium:4 parts Matrigel and allowed to solidify at 37˚C. Tumor slices were removed from RPMI
1086 and excess agarose was trimmed from slice edges (leaving a thin halo of agarose around slices
1087 to use for handling). Slices were spread across solidified Matrigel bed in 24 well plates. Rested T
1088 cells were stained with Violet Proliferation Dye 450 (BD Biosciences) diluted 1:1000 in PBS at 10
1089 x 10^6 cells/mL for 15 minutes at 37˚C. Cells were washed 2x with PBS and resuspended in T cell
1090 culture medium at 150 – 200 x 10^6 cells/mL. 5μL cell suspension (0.5 – 1 x 10^6 cells) was added
1091 directly on top of each slice and incubated at 37˚C for 3 hours, with 5μL fresh media added to
1092 each slice every 30 minutes to prevent slices from drying out. After incubation, 30μL non-diluted
1093 Matrigel was added directly atop each slice and allowed to solidify at 37˚C. 2mL T cell culture
1094 medium containing BME was added to each well. 1mL culture medium was removed and replaced
1095 with fresh medium every 24 hours throughout the experiment.

1096 **Single cell RNA Sequencing and Analysis:** Adoptively transferred CD45.1; OT-I; Cd69-TFP
1097 CD8 T cells were sorted from B78chOVA tumors d12 post transfer into four populations based on
1098 the CD69:TFP quadrants (Q1: TFP+/CD69-, Q2: TFP+/CD69+, Q3: TFP-/CD69-, and Q4: TFP-
1099 /CD69+). Cells were sorted from 8 tumors grown in separate mice and pooled by quadrants for
1100 barcoding and analysis. Sorted cells were separately labeled with lipid and cholesterol-modified
1101 oligonucleotides (LMO's) according to McGinnis et. al(*70*). Following 2 washes with PBS + 0.1%
1102 BSA, cells were pooled for encapsulation in one lane of a 10X 3' v3 kit with a target cell number
1103 of 18,000.

1104 Following construction of the GEX library (according to manufacturer's instructions) and the LMO
1105 library(*70*), libraries were pooled at a 10:1 molar ratio for sequencing on the NovaSeq 6000. This
1106 resulted in 807M cDNA reads and 163M LMO reads. Transcript and LMO reads were counted
1107 using the CellRanger count function against the GRCm38 reference genome to generate feature
1108 barcode matrices. These matrices were loaded into Seurat and filtered to remove high

1109 mitochondrial % cells (> 15%) and cells with low nGene (< 200 genes). Cells were then
1110 demultiplexed using their LMO counts with cells having too few LMO nUMI or ambiguous identity
1111 (possible multiplets) filtered out using the demultiplex package(*70*). The resulting object had an
1112 average cDNA nUMI per cell of 7662 reads and average nGene per cell of 2115 genes and
1113 average LMO nUMI per cell of 1080 reads. The final object underwent scaling and then scoring
1114 for cell cycle signatures (S and G2M scores as computed using Seurat's built-in CellCycleScoring
1115 function. The object then underwent regression for cell cycle effects (S and G2M score as
1116 described in the Seurat vignette) and percent mitochondrial reads before PCA. K-Means
1117 clustering and UMAP dimensional reduction was then performed on the first 16 PC's.

1118 To compare gene expression signatures of previously established subsets to the clusters in our
1119 dataset, we obtained the top 10 differentially expressed genes (sorted by log fold change and
1120 having an adjusted p-value <0.01) of T_{EX} clusters described in Daniel et al(*12*). Then we calculated
1121 gene expression scores corresponding to those subsets and mapped them onto the clusters in
1122 our data.

1123 **qRT-PCR:** At designated time points, CD8 T cells were isolated from the 96 well culture plates,
1124 or CD8 T cells were sorted into T cell media and centrifuged. The supernatant was aspirated out
1125 and the pellets stored at -80˚C until mRNA extraction using the RNEasy Micro Kit (Qiagen).
1126 Corresponding cDNA was synthesized from the mRNA samples using the cDNA amplification kit
1127 (Applied Biosystems). qPCR using pre-designed *Cd69* and *18s* probes (Invitrogen) with a
1128 TaqMan-based assay system (BioRad) or custom-made primers (iDT Technologies) for *Jun* (Fwd:
1129 5′ ACGACCTTCTACGACGATGC 3′, Rev: 5′ CCAGGTTCAAGGTCATGCTC 3′)(*71*) and *18s*
1130 (Fwd: 5' CTTAGAGGGACAAGTGGCG 3', Rev: 5' ACGCTGAGCCAGTCAGTGTA 3')(*72*) using
1131 the SsoFast assay system (BioRad) was used to quantify transcripts in a BioRad CFX94 machine.

1132 **Human tumor samples:** All tumor samples were collected with patient consent after surgical
1133 resection under a UCSF IRB approved protocol (UCSF IRB# 20-31740), as described

1134 previously(*63*). In brief, freshly resected samples transported in ice-cold DPBS or Leibovitz's L-
1135 15 medium before digestion and processing to generate a single-cell suspension. The following
1136 cancer indications were included in the cohort: Bladder cancer (BLAD), colorectal cancer (CRC),
1137 glioblastoma multiforme (GBM), gynecological cancers (GYN), hepatocellular cancers (HEP),
1138 head and neck cancer (HNSC), kidney cancer (KID), lung cancer (LUNG), melanoma (MEL),
1139 pancreatic ductal adenocarcinoma (PAAD), sarcoma (SRC).

1140 **Transcriptomic analysis of human tumors:** All tumor samples were collected under the UCSF
1141 Immunoprofiler project as described(*63*). Briefly, tumor samples were thoroughly minced with
1142 surgical scissors and transferred to GentleMACs C Tubes containing 800 U/ml Collagenase IV
1143 and 0.1 mg/ml DNase I in L-15/2% FCS per 0.3 g tissue. GentleMACs C Tubes were then installed
1144 onto the GentleMACs Octo Dissociator (Miltenyi Biotec) and incubated for 20 min (lymph node)
1145 or 35 min (tumor) according to the manufacturer's instructions. Samples were then quenched with
1146 15 mL of sort buffer (PBS/2% FCS/2mM EDTA), filtered through 100μm filters and spun down.
1147 Red blood cell lysis was performed with 175 mM ammonium chloride, if needed. Freshly digested
1148 tumor samples were sorted by FACS into conventional T cell, Treg, Myeloid, tumor and in some
1149 cases, stromal compartments and bulk RNA-seq was performed on sorted cell fractions. mRNA
1150 was isolated from sorted fractions and libraries were prepared using Illumina Nextera XT DNA
1151 Library Prep kit. The libraries were sequenced using 100bp paired end sequencing on HiSeq4000.
1152 The sequencing reads we aligned to the Ensembl GRCh38.85 transcriptome build using
1153 STAR(*73*) and gene expression was computed using RSEM(*74*). Sequencing quality was
1154 evaluated by in-house the EHK score, where each sample was assigned a score of 0 through 10
1155 based on the number of EHK genes that were expressed above a precalculated minimum
1156 threshold. The threshold was learned from our data by examining the expression distributions of
1157 EHK genes and validated using the corresponding distributions in TCGA. A score of 10
1158 represented the highest quality data where 10 out of 10 EHK genes are expressed above the

1159 minimum threshold. The samples used for survival analysis and other gene expression analyses
1160 had an EHK score of greater than 7 to ensure data quality. Ensemble gene signatures scores
1161 were calculated by converting the expression of each gene in the signature to a percentile rank
1162 among all genes and then determining the mean rank of all the genes in the signature.

1163 **Survival analysis:** Survival analyses using the TCGA dataset was performed using the TCGA
1164 sub-cohort described in (*63*). Briefly, tumor RNAseq counts and TPM along with curated clinical
1165 data for 13 cancer types (BLCA, COAD, GBM, GYN (grouping OV, UCEC and UCS), HNSC,
1166 KIRC, LIHC, LUAD, PAAD, SARC and SKCM) was filtered down to include primary solid tumors
1167 and metastatic samples only. This reduced the TCGA sample set to 4341 tumor samples. Q2 and
1168 Q4 gene scores (refer to the CITE-Seq section for details on the generation of the corresponding
1169 gene lists) were generated by first normalizing (using percentiles) the expression values of each
1170 gene composing the signature across all patients, followed by averaging these normalized values
1171 for each patient. We then calculated the ratio of Q2/Q4 gene scores for each patient. For survival
1172 analysis, patients were split into either or (Q2:Q4 gene signature ratio)^{HIGH} vs (Q2:Q4 gene
1173 signature ratio)^{LOW} (top/bottom 30% respectively, n=1291) and analyzed using a log-rank test.
1174 Similarly, the same Q2:Q4 ratio was used to stratify patients from the recent pan-cancer cohort
1175 with sorted T cell bulk RNA-Seq (*63*). Here, patients from the indications where Q2/Q4 ratio
1176 showed a prognostic benefit in the TCGA were combined together and those that did not were
1177 combined separately. Within each of these groups, T cell specific Q2/Q4 signature score ratio
1178 high and low were defined simply by the median of this ratio, and the survival of patient groups
1179 stratified in this way were tested by the log-rank test.
1180

1181 **Analysis from published datasets:** Available, curated RNA-Seq data (*8, 11, 23*) on *Cd69* and
1182 upstream transcription factor expression was plotted directly without modification.

1183 A curated R object derived from Zheng et al.(*62*) generously shared by Dr. Miguel Reina-Campos,
1184 UCSD, was used for analysis. Ensemble gene signatures were scored as mentioned above and
1185 plotted onto pre-existing UMAP dimensional reduction and already annotated cell clusters. While
1186 exhaustion genes were obtained from previously published work(*63*) ,*TCF7, SELL, LEF1, CCR7,*
1187 *IL7R* genes were used for the Naïve score. Q2 and Q4 expression scores (refer to the CITE-Seq
1188 section for details on the generation of the corresponding gene lists) were generated by the
1189 percentile scoring method as described above. Likewise, Ly108+CD69+ and Ly108+CD69- gene
1190 signatures were generated from gene lists corresponding to Signature 1 and Signature 7 from
1191 Beltra et al. 2020 (*11*) and the CD101-Tim3+ and CD101+Tim3+ gene lists were obtained from
1192 Hudson et al. (*13*) by filtering the top 25 by log fold change with p values <0.01. From these
1193 murine gene lists, some genes that did not have clear human orthologs or showed no expression
1194 in the Pan-cancer atlas dataset in question were excluded. Cells in the pan-cancer CD8 atlas
1195 were then gated by the ratio of Q2/Q4, Ly108+CD69+/Ly108-CD69+ and CD101-
1196 Tim3+/CD101+Tim3+ expression ratios (top and bottom 33% of the ratios) and queried for the
1197 expression of cytokine and exhaustion-related markers.

1198 The signatures of Myb cKO T_{EX} cells(*17*) and STAT5A over-expressed CD8 T cells(*37*) were
1199 derived by the same method using the top10 differentially expressed genes (by log fold change,
1200 with an adjusted p-value threshold <0.01). CD101-Tim3+, CD101+Tim3+ signatures were
1201 generated from published gene lists (*13*) as described above and the same procedure was
1202 followed for the circulating vs. resident signatures (*60*), in the latter taking the top 20 genes by log
1203 fold change and filtered by p-value <0.01. These were applied directly to the murine scSeq data
1204 sorted by Cd69:TFP quadrants.

1205 **In vitro Killing Assay:** MC38chOVA tumors with adoptively transferred Cd69-TFP-OT-I CD8 T
1206 cells in WT B6 mice were harvested at d8 post T cell transfer, digested as mentioned above, and
1207 sorted by CD69: TFP quadrants into cold T cell media. Sorted cells were centrifuged,

1208 resuspended in fresh, warm T cell media with BME and added onto MC38chOVA cells plated
1209 ~24h prior in flat-bottom 96 well plates. To each well containing 5000 MC38chOVA plated 24h
1210 prior, 5000 sorted T cells were added. As with the sort and restimulation experiments, each such
1211 collection of 5000 cells from a particular quadrant was pooled from 2-3 tumors and treated as a
1212 single biological replicate. Each experiment involved 7-8 tumors to obtain at least 3 biological
1213 replicates. Technical replicates were included and averaged wherever possible, i.e., at least
1214 10,000 cells were sorted from a given quadrant and biological replicate. Percentage killing was
1215 obtained by measuring the fractional loss of live cells at 36h in no T cell vs. T cell added conditions
1216 relative to 0h. Live cell numbers from each condition was accurately measured by lightly detaching
1217 cancer cells with trypsin and scoring against CountBright (ThermoFisher) absolute counting
1218 beads on a flow cytometer.

1219

1220 **CITE-Seq analysis of human tumors:** For CITE-Seq, post tumor digestion, cells were incubated
1221 with Human TruStain FcX Receptor Blocking Solution to prevent non-specific antibody binding
1222 before staining with Zombie Aqua Fixable Viability Dye and anti-human CD45 antibody in
1223 PBS/2%FCS/2mM EDTA/0.01% sodium azide and incubated for 25 min on ice in the dark. Live
1224 $CD45^+$ and CD45- cells were sorted on a BD FACSAria Fusion. $CD45^+$ and $CD45^-$ cells were
1225 pelleted and resuspended at 1x10^3 cells/ml in 0.04%BSA/PBS buffer before mixing in an 8:2
1226 CD45+:CD45- ratio and loaded onto the Chromium Controller (10X Genomics) to generate 5′ v1.1
1227 gel beads-in-emulsions (GEM). Pooled 8:2 CD45+:CD45- cells were resuspended in
1228 Cell Staining Buffer (BioLegend) and stained with a pool of 137 TotalSeq-C antibodies (Table)
1229 according to the manufacturer's protocol before loading onto the Chromium Controller (10X
1230 Genomics) for GEM generation. The cDNA libraries were generated using all or a subset of
1231 Chromium Next GEM Single Cell 5′ Library Kit for gene expression (GEX), Chromium Single Cell
1232 V(D)J Enrichment kit (10X Genomics) for T cell receptor (TCR), and Chromium Single Cell 5′

1233 Feature Barcode Library kit for antibody derived tag (ADT) according to the manufacturer's
1234 instructions. The libraries were subsequently sequenced on a Novaseq S4 sequencer (Illumina)
1235 to generate fastqs with the following mean reads per cell: 42,000 (GEX), 34,000 (TCR), and 5,700
1236 (ADT). For multimodal clustering and analysis, CLR normalization followed by weighted nearest
1237 neighbor (WNN) clustering was performed using the Seurat package in R. Naïve and Exhaustion
1238 scores were generated using the percentile rank method as mentioned above, but with protein
1239 (ADT) markers- Naïve : CD62L, CD45RA, IL7RA; Exhaustion: PD-1, CTLA-4, CD38, CD39.
1240 Progenitor and Effector scores were generated from human orthologs of murine gene signatures
1241 (top 20 genes by log fold change) in Daniel et al. (*12*), removing those genes that have no
1242 expression in this dataset or no human equivalent. To compare cluster identities across datasets,
1243 we obtained gene signatures from the DEGs for each of our clusters and mapped their expression
1244 on to each major subset in a published pan-cancer intratumoral T cell atlas(*62*).

1245 Q2 and Q4 gene signatures were generated by DEG of all intratumoral CD8 T cells belonging in
1246 these groups with a log fold change threshold of 0.25 and filtered by a p-value <0.01. For analysis
1247 of expression of various markers (*JUN, IFNG,* Exhaustion score) between Q2 and Q4, we select
1248 for those samples with at least 50 cells in a group to offer reliable metrics. This filters out certain
1249 patient samples when quantifying the same metrics within Tex^{Early} and Tex^{Late} subsets.

1250

1251 **Live 2-photon imaging of tumor slices and image analysis:** Live imaging of tumor slices was
1252 performed on a custom-made 2-photon microscope as previously described(*1*). Briefly, 1 million
1253 CD2dsRed; OT-I; Cd69-TFP or control CD2dsRed; OT-I CD8 T cells were retro-orbitally injected
1254 into WT mice bearing MC38chOVA tumors injected 5-7d earlier and harvested 7-10d after T cell
1255 injection. Slices for imaging were generated as described above for the ex vivo slice culture assay.
1256 Slices were placed in a custom-made perfusion chamber and imaged under oxygenated and
1257 temperature-controlled perfusion of RPMI 1640, as described previously(*1*). Dual laser excitations

at 825nm and 920nm were used to excite the requisite fluorophores. Image analysis was performed on Imaris (BitPlane) with custom-made plugins developed on Matlab (Mathworks) and Fiji. Surfaces were generated on CD8 T cells and in both CD2dsRed; OT-I and CD2dsRed; OT-I; Cd69-TFP bearing slices and the corresponding levels of the former in the 515-545nm range PMT were used to gate on TFP^{hi} vs. TFP^{lo} OT-Is.

Cell tracking was performed on Imaris and corresponding cell positions imported to Matlab for further analysis to fit the persistent random walk model (PRWM) to the cell trajectories(*75*) using the method of overlapping intervals (*76*). Briefly, the mean squared displacement (MSD) for a cell for given time interval t_i was obtained from the average of all squared displacements x_{ik} such that

$$\overline{x_i} = \frac{1}{n_i}\sum_{k=1}^{n_i} x_{ik} \quad (1)$$

and

$$n_i = N - i + 1 \quad (2)$$

where n_i is the number of overlapping time intervals of duration t_i and N the total number of time intervals for the experiment. Mathematically, the persistent random walk model can be written as

$$MSD(t) = n_d S^2 P[t - P\left(1 - e^{-\frac{t}{P}}\right)] \quad (3)$$

where S is the migration speed and P is the persistence time. The motility coefficient is given as

$$\mu = S^2 P \quad (4)$$

where n_d is the dimensionality of the random walk (in this case n_d=3). We fitted the PRWM in 3D to obtain estimates of speed, persistence time and motility of each cell track by non-linear regression.

Statistical Analysis: Statistical analysis was done in GraphPad Prism or in R. For testing null hypothesis between two groups, either Student's t tests and or the non-parametric Mann-Whitney

1281 U tests were used, depending on the number and distribution of data points. Likewise, for testing
1282 null hypotheses among 3 or more groups, ANOVA or non-parametric tests were performed,
1283 followed by post-hoc Holm-Sidak's test, correcting for multiple comparisons. Unless otherwise
1284 mentioned, data are representative of at least 2 independent experiments.

1285

Supplementary Figures:

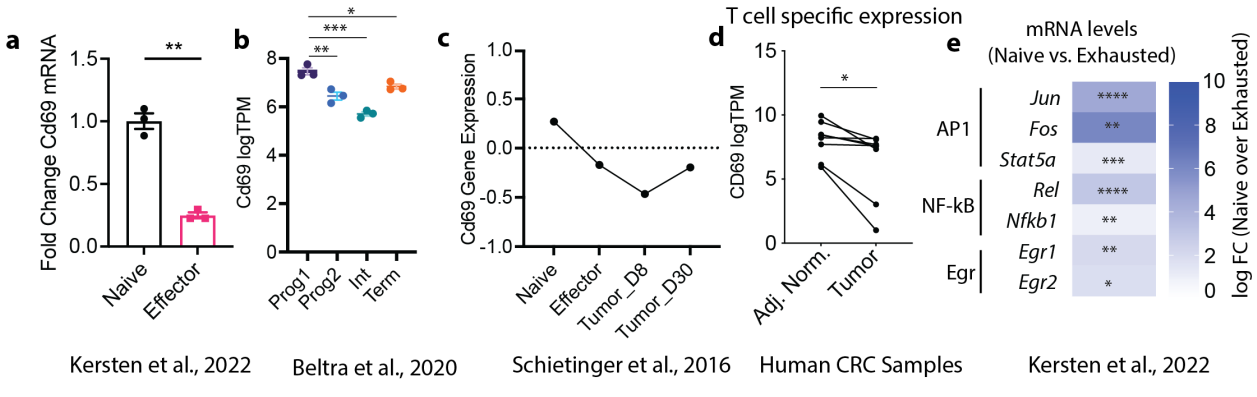

Fig. S1: **Resting Cd69 mRNA decreases with T cell differentiation towards exhaustion.** Cd69 mRNA expression in **(a)** Naïve vs. in vitro generated (stimulation with Dynabeads followed by rest in IL-2 containing media) effector CD8 T cells from published RNASeq data(*23*); **(b)** Progenitor and exhausted T cell subsets from published data (*11*), **(c)** among Naïve, Effector, D8 tumor and D30 tumor infiltrating T cells from other published data (*8*), **(d)** in conventional T cells sorted from tumor and adjacent normal regions of human colorectal cancer patients; **(e)** depressed mRNA expression of factors associated with the Cd69 transcription in Naïve vs. Exhausted CD8 T cells from previous work (*23*) (symbols indicate FDR adjusted p-values). Plots show mean +/- SEM (a, b) p-values obtained by unpaired (a) and paired Student's t test (d), and by ANOVA followed by post-hoc Tukey test. *p< 0.05, **p<0.01, ***p<0.001, ****p<0.0001.

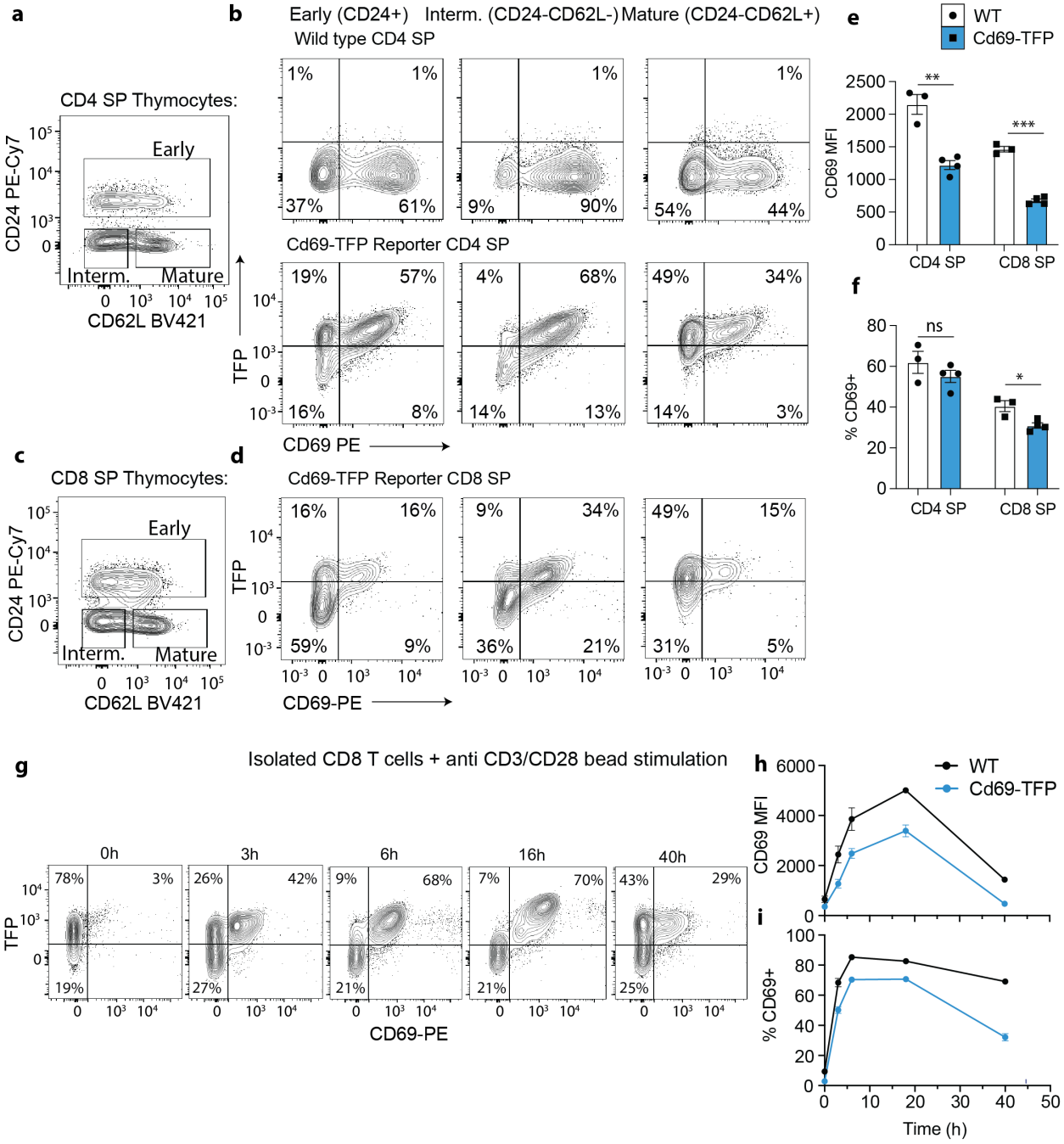

Fig. S2: Cd69 transcriptional reporter TFP is expressed along with surface CD69 protein in known contexts of TCR stimulation. **(a, c)** Representative flow cytometry plot of CD62L and CD24 expression in **(a)** CD4+CD8- (CD4 single positive or SP) and **(c)** CD8+CD4- or CD8 SP thymocytes to demarcate early, intermediate (interm.) and mature subsets; **(b, d)** corresponding flow cytometry plots of TFP and CD69 expression in these subsets with varying degree of maturity in **(b)** CD4 SP cells in Cd69-TFP mice along with WT mice as controls and **(d)** in CD8 SP cells in Cd69-TFP reporter mice (WT: circular points, white bar; Reporter: square points, blue bars); quantification of **(e)** CD69 MFI and **(f)** %CD69+ in CD4 SP and CD8 SP cells from WT and Cd69-TFP reporter mice; **(g)** Representative flow cytometry plots of TFP vs. CD69 of isolated CD8 T cells from lymph nodes and spleen? Of an unchallenged reporter mouse at different time points

post stimulation with αCD3+αCD28 Dynabeads and corresponding quantification of **(h)** CD69 MFI and **(i)** %CD69+ in these stimulated CD8 T cells from WT and Cd69-TFP reporter mice. *p< 0.05, **p<0.01, ***p<0.001, ns = no significance.

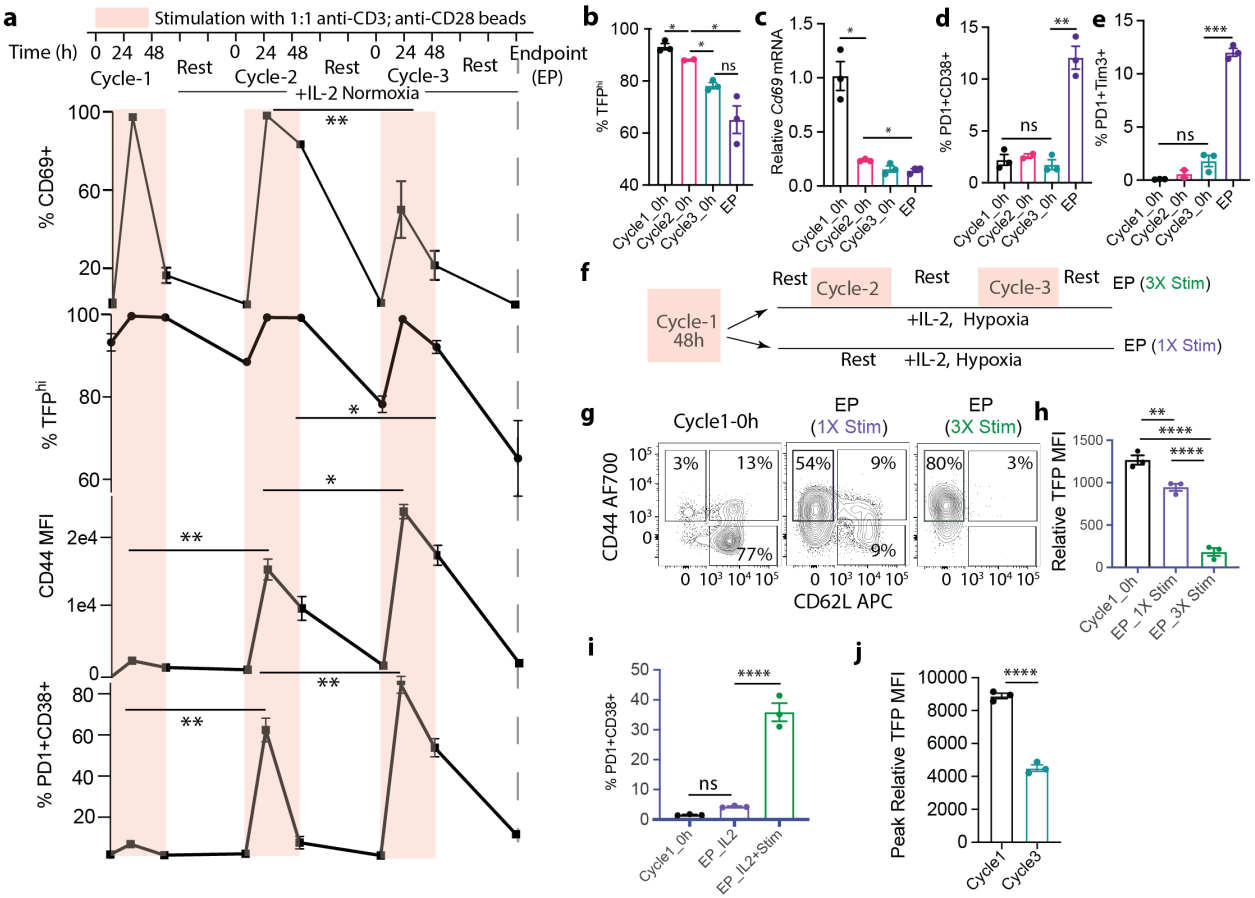

Fig. S3: Repeated TCR stimulation drives down TFP with acquisition of exhaustion markers (a) %CD69+, %TFP^{hi}, CD44 MFI, %PD1^{+}CD38^{+} of freshly isolated CD8 T cells through successive cycles of 48h stimulation and 72h resting in ambient oxygen (normoxia) + IL-2; **(b)** %TFP^{hi}, **(c)** *Cd69* mRNA by qPCR and **(d)** %PD1^{+}CD38^{+}, **(e)** %PD1^{+}Tim-3^{+} at the beginning of cycles 1, 2, 3 and endpoint (EP); **(f)** experimental schematic showing 1X Stim vs. 3X Stim conditions to parse the role of stimulation vs. IL-2 alone; **(g)** flow cytometry plots showing representative CD44 vs. CD62L profiles of CD8 T cells at the timepoints and conditions indicated; for the same experiment, **(h)** TFP (relative to WT control), **(i)** %PD1^{+}CD38^{+} of CD8 T cells at the starting point (Cycle1_0h) and at endpoint (EP) either with 1X Stim followed by prolonged rest or 3X stim; **(j)** Peak Relative TFP and CD69 MFI between Cycle 1 and Cycle 3 in normoxia; Bar graphs represent mean +/- SEM; null hypothesis testing by ANOVA followed by post-hoc Holm-Šídák test; data representative of 2 independent experiments, each with 3 mice and technical duplicates/biological replicate at every assay point. *p< 0.05, **p<0.01, ***p<0.001, ****p<0.0001, ns = no significance.

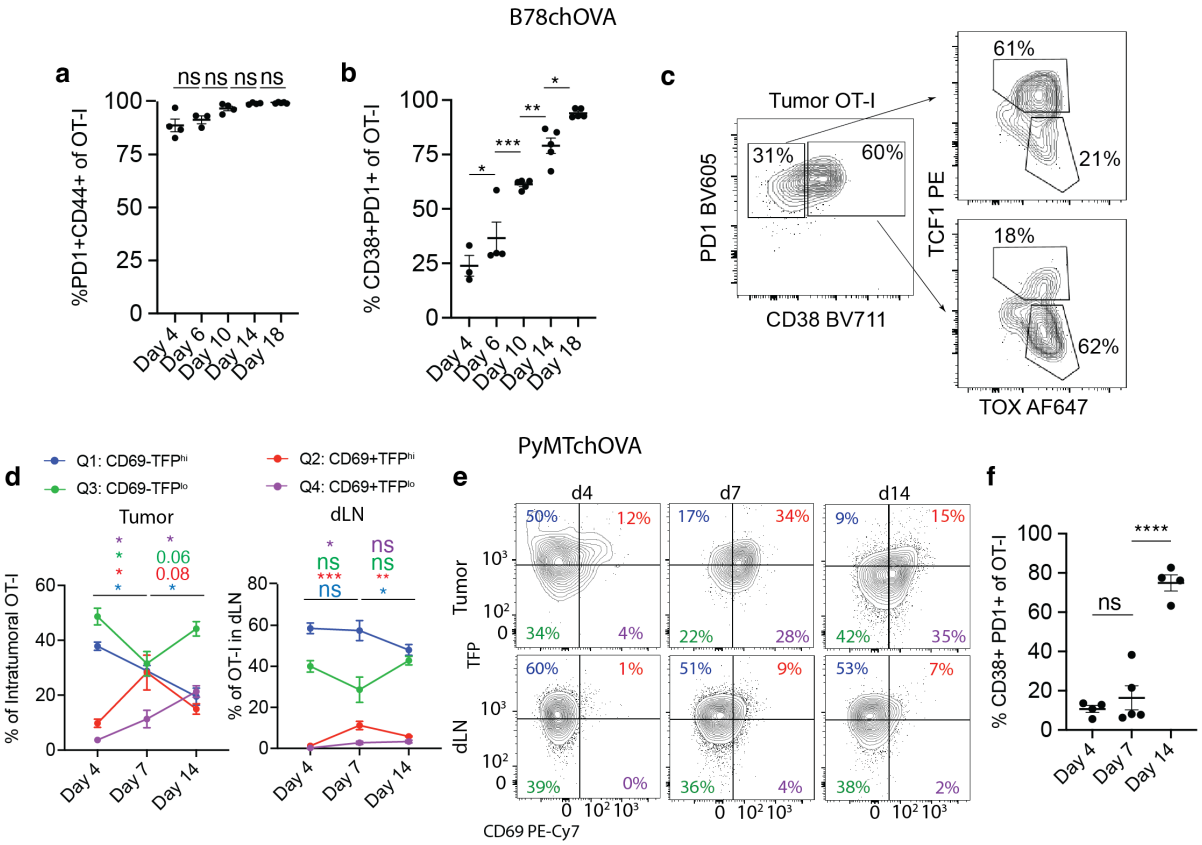

Fig. S4: TFP decrease accompanies antigen-specific CD8 T cell residence time in TME: (a) %PD1+CD44+ and **(b)** %PD1+CD38+ of intratumoral OT-I CD8 T cells at different time points after adoptive transfer into WT mice bearing B78chOVA tumors; **(c)** Flow cytometry plots showing TCF1 and TOX expression in PD1+CD38- and PD1+CD38+ intratumoral OT-Is d14 post adoptive transfer in the same tumors; (**d)** CD69:TFP quadrant (Q1-Q4) distribution for OT-I T cells in the tumor and tdLN over time after adoptive transfer into PyMTchOVA mice bearing mammary tumors**; (e)** corresponding corresponding flow cytometry plots showing TFP and CD69 expression of the same adoptively transferred OT-I T cells; **(f)** %PD1+CD38+ of intratumoral OT-I CD8 T cells at different time points after adoptive transfer into PyMTchOVA mice bearing mammary tumors. Bar graphs show mean +/- SEM. *p<0.05, **p<0.01, ***p<0.001, ****p<0.0001, 0.05<p<0.1 are recorded, ns: p>=0.1, by one-way ANOVA with post-hoc Holm-Sidak multiple comparison test for a, b, f and 2-way ANOVA with post-hoc Tukey test between pair-wise timepoints in (d).

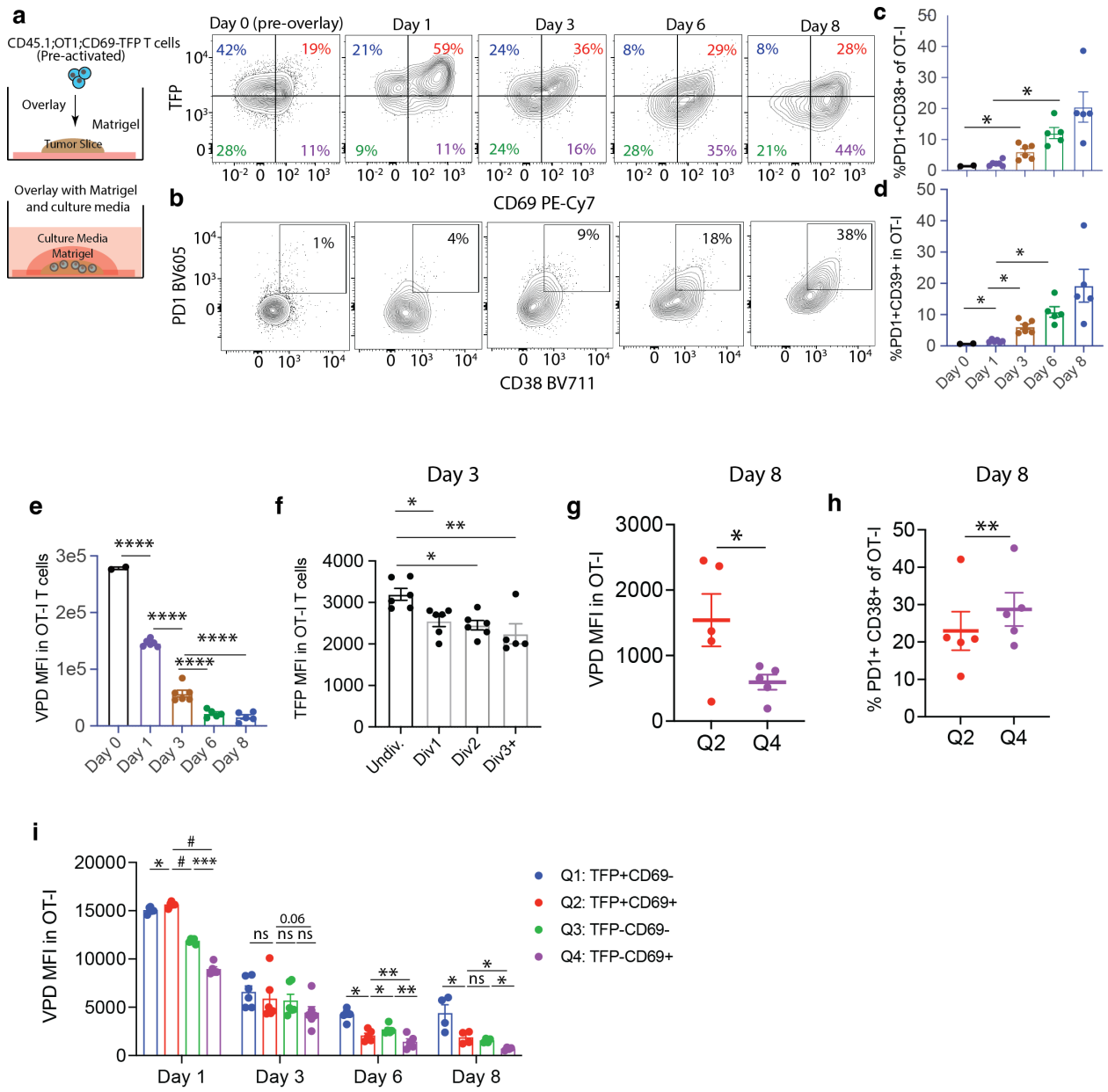

Fig. S5: Ex vivo tumor slice overlay culture mimics OT-I differentiation in vivo: Schematic of tumor slice culture assay with representative flow cytometry plots of **(a)** TFP vs. CD69 and **(b)** PD1 vs. CD38 expression in slice-internal OT-I T cells from Day1-Day8, compared to Day0 (pre-overlay); **(c)** %PD1+CD38+, **(d)** %PD1+CD39+ and **(e)** Violet proliferation dye (VPD) MFI of Day 0 pre-overlay and slice-internal OT-I T cells at different time points after slice overlay (Day1-Day8); **(f)** bar graph showing TFP MFI of slice OT-I T cells by estimated number of divisions (>=3, 2, 1, or divided) at Day 3; **(g)** VPD MFI and **(h)** %PD1+CD38+ of slice-internal OT-Is from Q2 and Q4 at Day8; **(i)** VPD MFI by CD69:TFP quadrants over time in OT-I T cells recovered from within slices; Bar graphs show mean +/- SEM, null hypothesis testing by ANOVA and post hoc Holm-Šídák test (c-f), or paired t test in g, h, 2-way ANOVA and multiple comparison tests controlling for False Discovery Rates (i); data are representative of 2 independent experiments, each 5-6 slices/time point for each slice experiment and Day 0 pre-overlay samples in duplicate; TFP gated

on OT-I control (without Cd69-TFP) CD8 T cells. *p< 0.05, **p<0.01, ***p<0.001, **** or #p<0.0001.

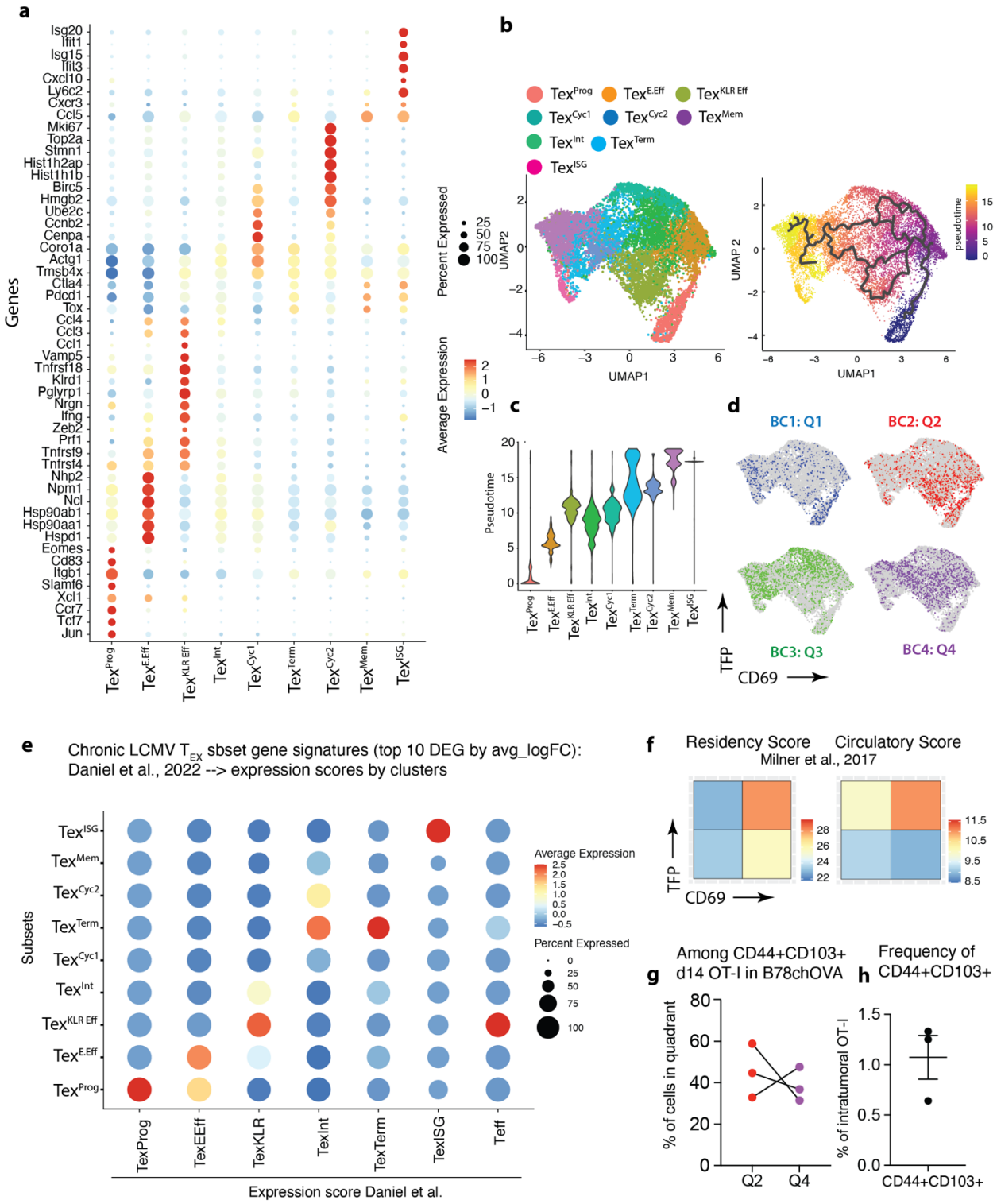

Fig. S6: Gene expression based clustering of intratumoral OT-Is and relationship to Cd69 transcription (a) Dotplot representation of differentially expressed and canonical T_{EX}-associated genes across the computationally derived cell clusters from the scSeq of intratumoral Cd69-TFP:OT-I CD8 T cells at d12 post injection into B78chOVA tumor-bearing mice; **(b)** UMAP representation of the scSeq data color-coded by pseudotime derived from Monocle3 trajectory analysis and **(c)** Pseudotime spread of each cluster from the same analysis; **(d)** overlay of cells with barcodes corresponding to the sorted CD69:TFP clusters in the UMAP space; **(e)** Average expression of the signature scores from top 10 DEGs of LCMV-derived T_{EX} clusters from Daniel et al.(*12*) in the subsets obtained from this study; **(f)** Expression score derived from transcriptomic signatures of CD8 T cell residency vs. circulation, as defined by Milner et al., 2017 ; **(g)** distribution in Q2 vs. Q4 quadrants and **(h)** frequency of CD44+CD103+ T_{RM}-like cells in adoptively transferred d14 OT-I T cells in B78chOVA tumors.

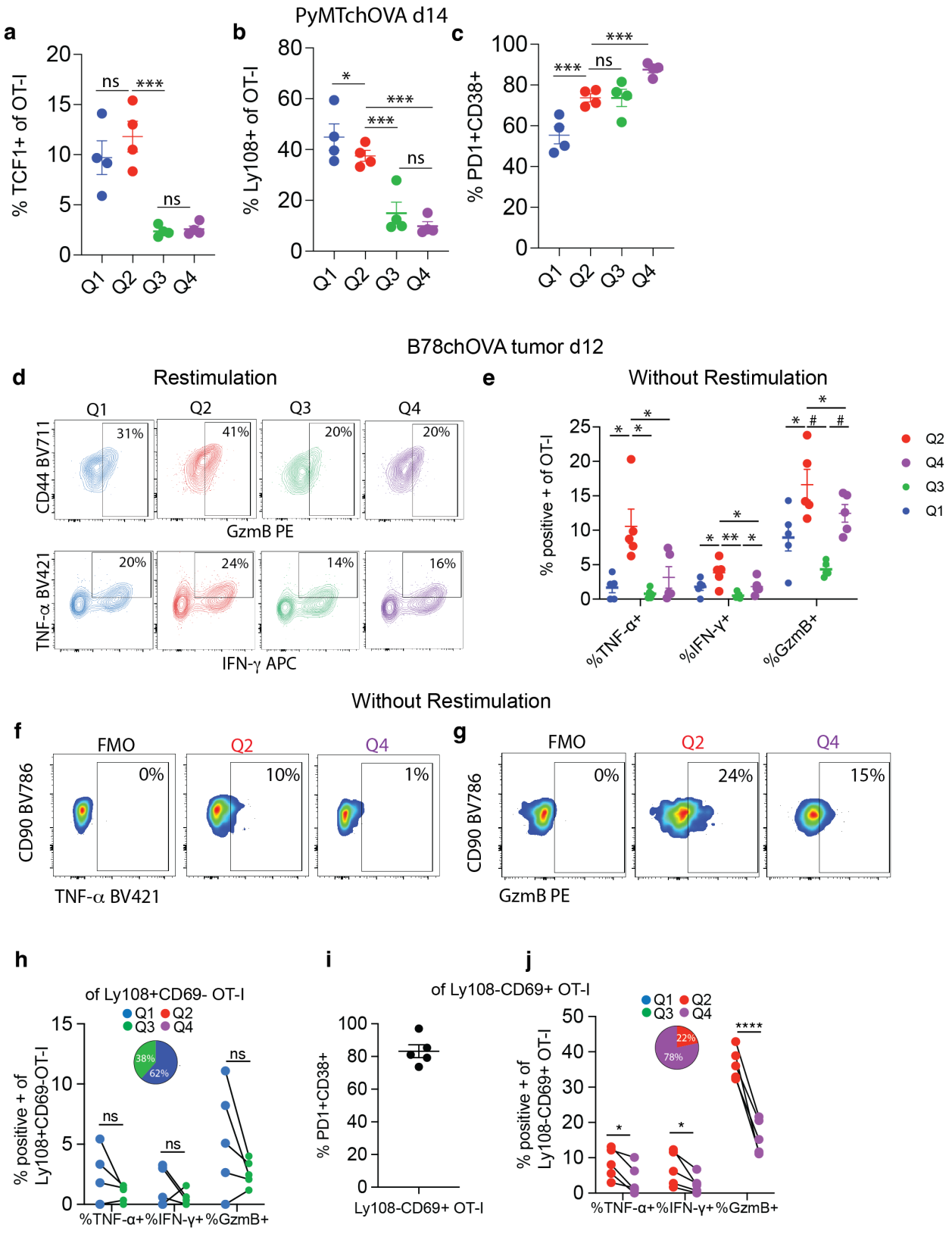

1373

1374 **Fig. S7: (a)** % TCF1+, **(b)** %Ly108+, **(c)** %PD1^{+}CD38^{+} of intratumoral OT-I T cells grouped by
1375 CD69:TFP quadrants in PyMTchOVA mammary tumors 14d post-adoptive transfer; **(d)**

representative flow cytometry plots showing TNF-α, IFN-γ and GzmB expression in intratumoral OT-I T cells in B78chOVA tumors 12d post adoptive transfer by Cd69:TFP quadrants, assayed directly by intracellular staining without sort and restimulation; **(e)** quantification of TNF-α, IFN-γ and GzmB expression of the same intratumoral OT-I T cells, sorted by Cd69:TFP quadrants and restimulated for 3h with PMA/ionomycin; flow cytometry plots showing intracellular **(f)** TNF-α and **(g)** GzmB expression in intratumoral OT-I T cells 12d post adoptive transfer into B78chOVA tumors**;** cytokine and GzmB expression of Q2 vs. Q4 OT-I T cells within **(h)** Ly108+CD69-(*11*) and **(j)** Ly108-CD69+(*11*) subsets with inset pie chart showing the percentage of cells in each quadrant within the corresponding subsets; **(i)** %PD1^{+}CD38^{+} among Ly108-CD69+ intratumoral OT-Is; graphs represent mean +/- SEM; null hypothesis testing by RM ANOVA followed by post-hoc paired t-tests corrected for multiple comparisons; *p< 0.05, **p<0.01, ***p<0.001, ****p<0.0001, ns = no significance, #p<0.001 in (e).

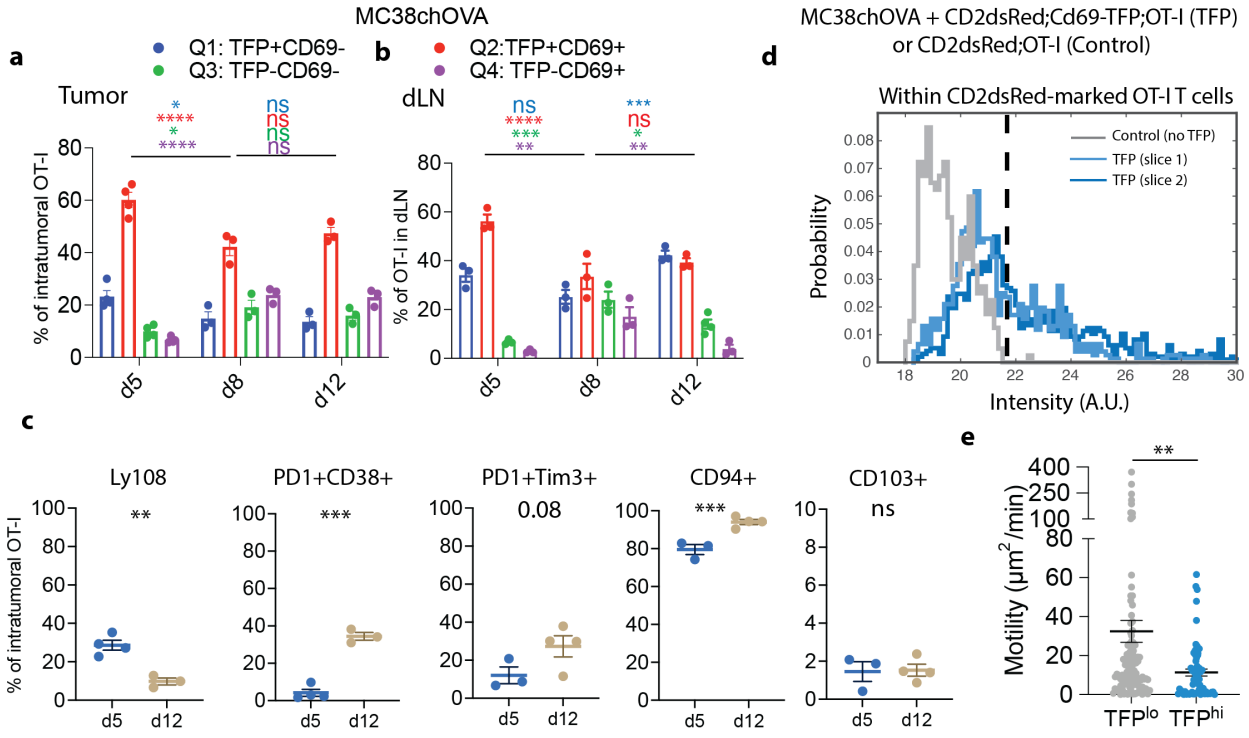

Fig. S8: Bar graphs showing TFP:CD69 quadrant distribution among OT-I CD8 T cells in **(a)** tumors and **(b)** corresponding tdLN at d5, d8, d12 post T cell injection into MC38chOVA tumor-bearing mice (n=3-4 mice per group respectively); **(c)** expression of surface markers of progenitor, exhausted, effector and T_{RM}-like states in intratumoral OT-Is (d5 and d12) in MC38chOVA tumors; **(d)** Representative histograms of channel intensity within OT-I T cells in live tumor slices to find TFP^{hi} cells using CD2dsRed and CD2dsRed;Cd69-TFP OT-Is; **(e)** overall 3D motility of TFP^{hi} vs. TFP^{lo} intratumoral OT-Is d8 post adoptive transfer within live MC38chOVA tumor slices; bar graphs show mean +/- SEM, null hypothesis testing by Mann-Whitney U test (e), 2-way ANOVA with post-hoc Tukey test between pair-wise timepoints (a, b) and unpaired t tests (c). *p< 0.05, **p<0.01, ***p<0.001, ****p<0.0001, ns = no significance.

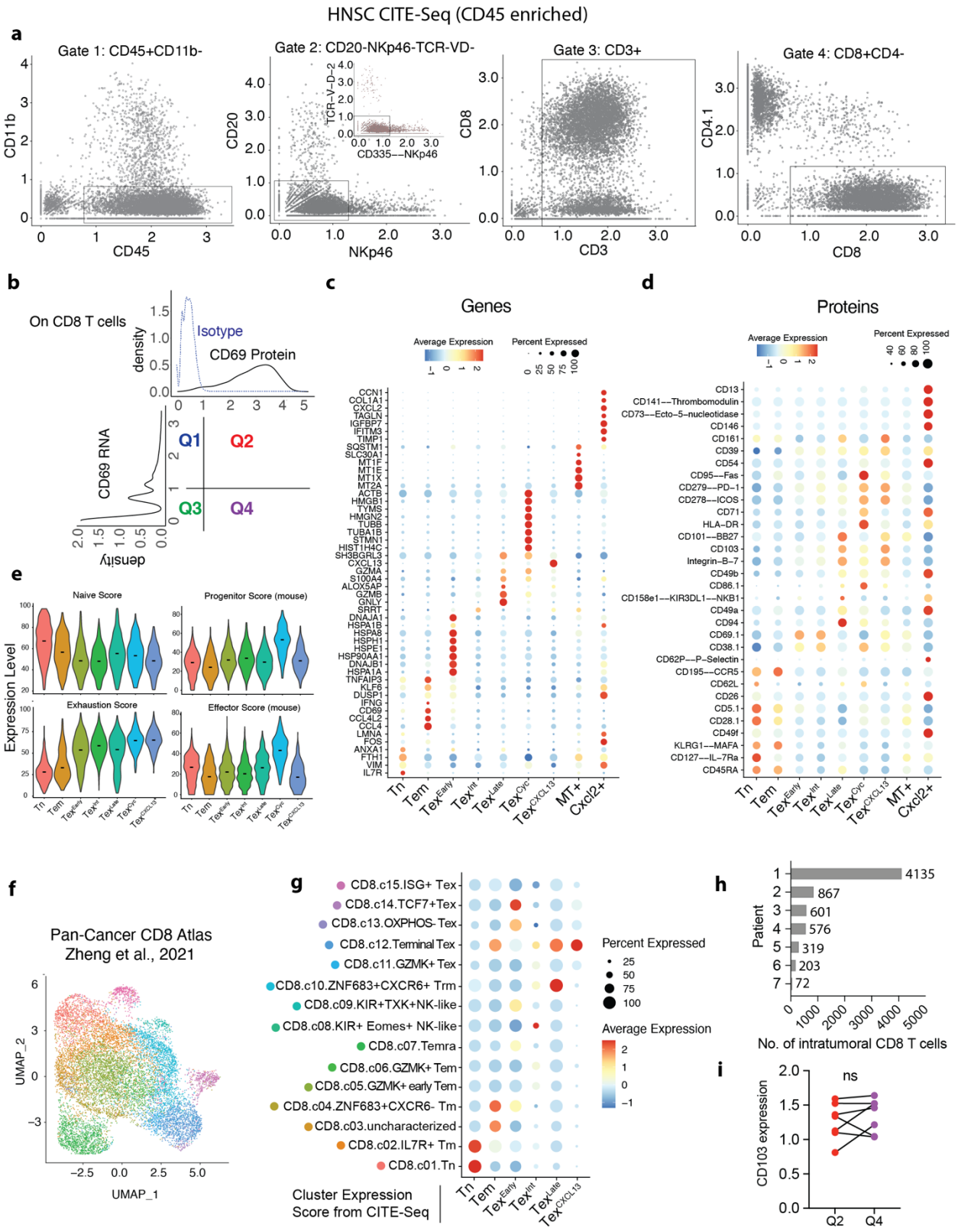

1401

1402 **Fig. S9**: **CITE-Seq of HNSC tumor allows mapping of Cd69 RNA:CD69 Protein quadrants**
1403 **onto CD8 T cell phenotypes (a)** Gating scheme of CD45-enriched CITE-Seq from HNSC patient

data using protein markers to isolate a pure CD8 T cell population; **(b)** Gating of the CD8 T cell population into CD69 Protein: CD69 RNA quadrants (Q1-Q4) ; **(c)** DEGs and **(d)** DE antibody-tagged surface proteins for the computationally derived subsets obtained through multimodal clustering using both protein and RNA; **(e)** progenitor and effector scores derived from (*12*) along with naïve and exhaustion scores (based on antibody-derived tags as in Fig. 6c). **(f)** UMAP representation of computationally-derived subsets among CD8 T cells in a pan-cancer T cell atlas(*62*), color-coded subset labels are as shown in (g); **(g)** DEGs from each subset in the CITE-Seq data (avg_logFC>0.5, adj_pvalue <0.01) were used to generate gene signature scores and mapped onto the major pan-cancer CD8 T cell subsets; **(h)** Number of CD8 T cells recovered by gating in a from each patient in the CITE-Seq data; **(i)** CD103 (antibody-tagged) expression among Q2 and Q4 (gated as in b) intratumoral CD8 T cells from CITE-Seq, ns: no significance by paired t-test.

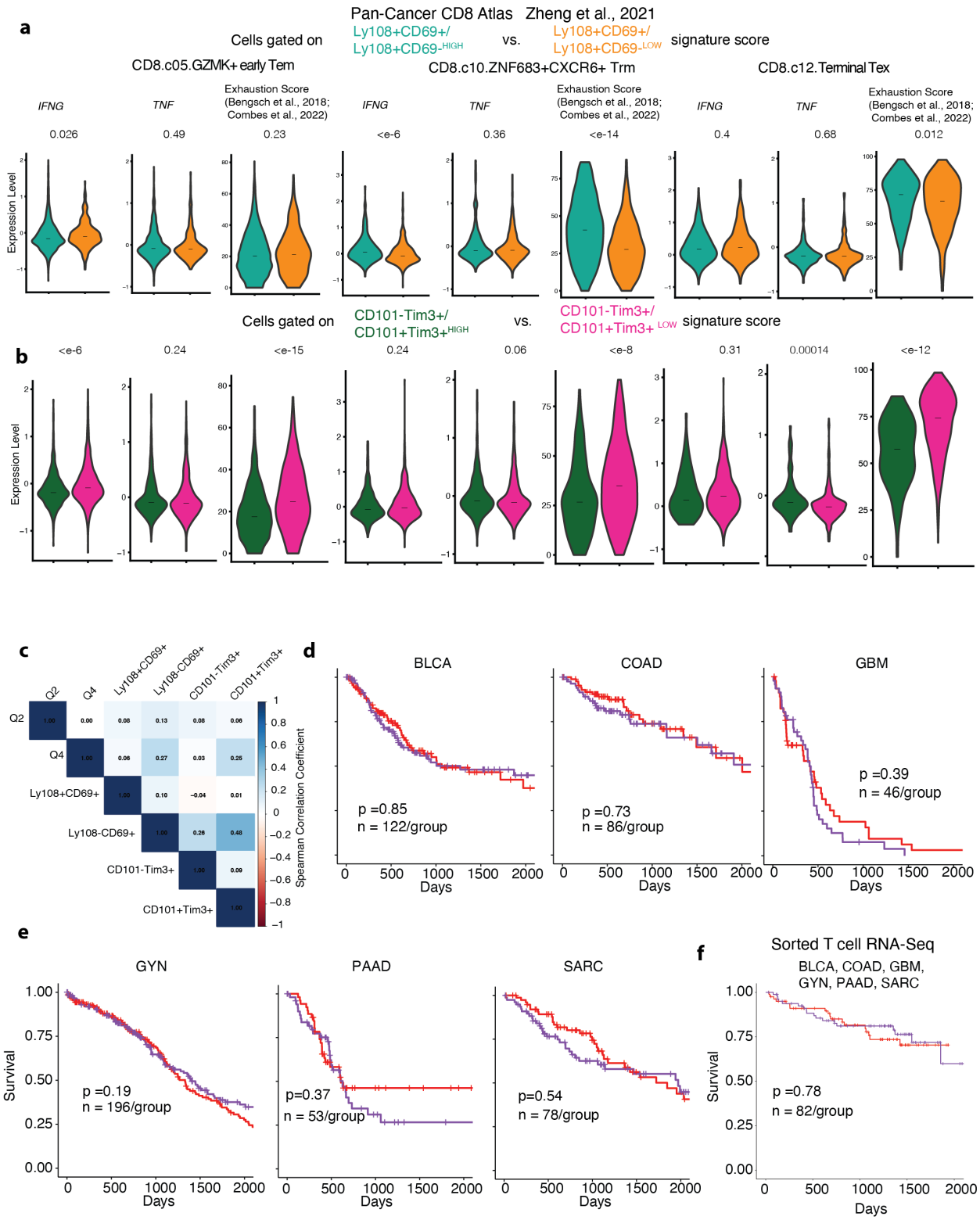

Fig. S10: **(a, b)** expression of *IFNG*, *TNF* and Exhaustion signature score within the Early Tem, CXCR6+ Trm and Terminal Tex clusters from the Pan-Cancer CD8 atlas (Zheng et al., 2021), grouped by signatures corresponding to **(a)** the ratio of Ly108+CD69+ and Ly108-CD69+ expression scores (Signature 1 and Signature 7 from (*11*), and **(b)** the ratio of expression scores

1422 for the CD101-Tim3+ effector and CD101+Tim3+ terminal subsets (*13*); **(c)** Spearman correlation
1423 matrix showing the relationship among the used gene signatures, Q2 and Q4 from this study,
1424 Signature 1 (Ly108+CD69+), Signature 7(Ly108-CD69+) from (*11*), CD101-Tim3+ and
1425 CD101+Tim3+ from (*13*); Kaplan-Meier survival curves from a quality controlled subset of TCGA
1426 data (*63*) corresponding to **(d)** BLCA, COAD, GBM, **(e)** GYN, PAAD and SARC indications,
1427 patients stratified by the ratio of Q2 and Q4 expression scores; **(f)** Kaplan-Meier survival curves
1428 from a cohort of patients of combined BLCA, COAD, GBM, GYN, PAAD, SARC indications, with
1429 patients stratified by the ratio of Q2 and Q4 expression scores from bulk RNA-Seq of sorted T
1430 cells(*63*) number of patients per group (after stratification) and p-value for log-rank tests are noted
1431 in each panel.

1432